Nano-Micro Letters

e-ISSN 2150-5551
CN 31-2103/TB

ARTICLE

https://doi.org/10.1007/s40820-025-01845-7

Cite as
Nano-Micro Lett.
(2025) 17:329

Received: 21 March 2025
Accepted: 15 June 2025

Core–Shell IrPt Nanoalloy on La/Ni–Co_3O_4 for High-Performance Bifunctional PEM Electrolysis with Ultralow Noble Metal Loading

Yifei Liu[1,2], Xinmeng Er[3], Xinyao Wang[4], Hangxing Ren[1,2], Wenchao Wang[1,2], Feng Cao[1,2], Taiyan Zhang[1,2], Pan Liu[4], Yakun Yuan[1,6], Fangbo Yu[7], Yang Ren[5], Fuqiang Huang[1,2] ✉, Wenjiang Ding[1] ✉, Lina Chong[1,2] ✉

HIGHLIGHTS

- Core–shell IrPt nanoalloy on La/Ni–Co_3O_4 achieves unprecedented bifunctional activity (2 A cm^{-2} at 1.72 V) in proton exchange membrane water electrolysis (PEMWE) with ultralow loadings (0.075 mg cm^{-2} Ir/Pt at both electrodes).
- 646-h durability in PEMWE cell (5 μV h^{-1} decay) via IrPt-core@$IrPtO_x$-shell synergy, hierarchical pores, and oxygen vacancies for robust electron/mass transfer and active-site stability.
- In situ X-ray absorption spectroscopy combined with density functional theory unveils Ir–O–Pt sites enabling bi-nuclear oxygen evolution reaction and Volmer–Tafel hydrogen evolution reaction mechanisms through optimized Ir/Pt charge redistribution, breaking kinetic limitations.

ABSTRACT The development of highly efficient and durable bifunctional catalysts with minimal precious metal usage is critical for advancing proton exchange membrane water electrolysis (PEMWE). We present an iridium–platinum nanoalloy (IrPt) supported on lanthanum and nickel co-doped cobalt oxide, featuring a core–shell architecture with an amorphous IrPtOx shell and an IrPt core. This catalyst exhibits exceptional bifunctional activity for oxygen and hydrogen evolution reactions in acidic media, achieving 2 A cm^{-2} at 1.72 V in a PEMWE device with ultralow loadings of 0.075 mg_{Ir} cm^{-2} and 0.075 mg_{Pt} cm^{-2} at anode and cathode, respectively. It demonstrates outstanding durability, sustaining water splitting for over 646 h with a degradation rate of only 5 μV h^{-1}, outperforming state-of-the-art Ir-based catalysts. In situ X-ray absorption spectroscopy and density functional theory simulations reveal that the optimized charge redistribution between Ir and Pt, along with the IrPt core–IrPtOx shell structure, enhances performance. The Ir–O–Pt

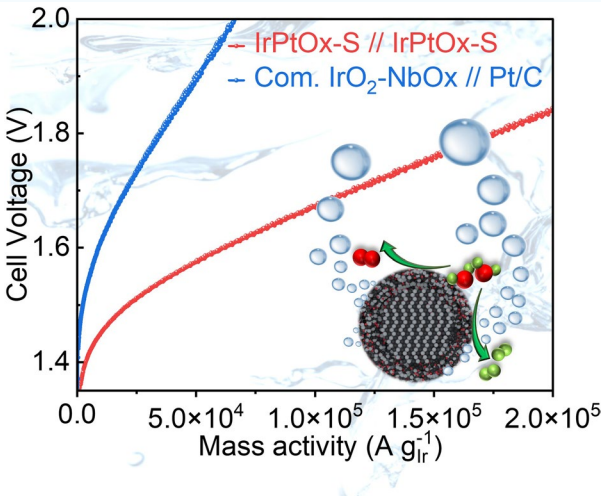

✉ Fuqiang Huang, huangfq@sjtu.edu.cn; Wenjiang Ding, wjding@sjtu.edu.cn; Lina Chong, chonglina@sjtu.edu.cn
[1] Center of Hydrogen Science, School of Materials Science and Engineering, Shanghai Jiao Tong University, Shanghai 2000240, People's Republic of China
[2] Zhangjiang Institute for Advanced Study (ZIAS), Shanghai Jiao Tong University, Shanghai 201210, People's Republic of China
[3] State Key Laboratory for Mechanical Behavior of Materials, School of Materials Science and Engineering, Xi'an Jiao Tong University, Xi'an 710049, People's Republic of China
[4] State Key Laboratory of Metal Matrix Composites, Shanghai Jiao Tong University, Shanghai 200240, People's Republic of China
[5] Department of Physics, JC STEM Lab of Energy and Materials Physics, City University of Hong Kong, Kowloon Tong 999077, Hong Kong, People's Republic of China
[6] School of Mechanical Engineering, Shanghai Jiao Tong University, Shanghai 200240, People's Republic of China
[7] International Research Center for Renewable Energy, State Key Laboratory of Multiphase Flow in Power Engineering, Xi'an Jiao Tong University, Shaanxi 710049, People's Republic of China

Published online: 14 July 2025

active sites enable a bi-nuclear mechanism for oxygen evolution reaction and a Volmer–Tafel mechanism for hydrogen evolution reaction, reducing kinetic barriers. Hierarchical porosity, abundant oxygen vacancies, and a high electrochemical surface area further improve electron and mass transfer. This work offers a cost-effective solution for green hydrogen production and advances the design of high-performance bifunctional catalysts for PEMWE.

KEYWORDS Proton exchange membrane water electrolysis; Bifunctional catalyst; Oxygen evolution reaction; Hydrogen evolution reaction; Core–shell catalyst

1 Introduction

The transition to a sustainable energy future hinges on the development of efficient technologies for green hydrogen production, with proton exchange membrane water electrolysis (PEMWE) emerging as a leading candidate [1]. PEMWE offers a promising pathway to convert and store renewable energy, addressing the global energy crisis and advancing carbon neutrality goals [2–6]. However, the widespread adoption of PEMWE is hindered by the reliance on precious group metals (PGMs), such as platinum (Pt) and iridium (Ir), which are scarce, expensive, and subject to supply chain constraints [7]. Currently, Pt and Ir remain the materials of choice for the hydrogen evolution reaction (HER) and oxygen evolution reaction (OER), respectively, due to their optimal balance of electrocatalytic activity and durability under the harsh acidic and corrosive conditions of PEMWE [8]. Nevertheless, typical Pt loadings at the cathode (~0.4 mg cm^{-2}) and Ir loadings at the anode (2–4 mg cm^{-2}) far exceed the U.S. Department of Energy (DOE) 2026 target of reducing total PGM loading to < 0.5 mg cm^{-2} without compromising performance [9, 10].

The development of bifunctional catalysts capable of catalyzing both OER and HER has gained significant attention, as they simplify electrode manufacturing and reduce costs [11–15]. However, designing such catalysts with significantly reduced PGM loadings while maintaining high activity and stability remains a formidable challenge, particularly under the extreme chemical and electrochemical conditions of PEMWE [16, 17]. While Pt is the most effective HER catalyst, it performs poorly for OER due to the formation of non-conductive PtO_2 under high-voltage conditions, which increases surface resistivity ($\rho PtO_2 \approx 10^6$ Ω cm) and reduces activity [18–20]. In contrast, Ir oxides exhibit metallic conductivity, with resistivity approximately 11 orders of magnitude lower than that of Pt oxides, making them more suitable for OER [21]. However, Ir-based catalysts are less effective for HER. To overcome these limitations, researchers have explored Pt–Ir bimetallic systems, which leverage synergistic interactions between Pt and Ir to enhance catalytic activity. For example, Pt nanoparticles dispersed on IrO_2 supports, or IrO_2 formed on Pt black surfaces, have demonstrated excellent bifunctional activity for both OER and HER in three-electrode systems [22–24]. Yim et al. evaluated a series of bifunctional catalysts, including Pt, Pt–Ir, Pt–Ru, and Pt–Ru–Ir, and found that Pt–Ir exhibited the best overall activity, stability, and round-trip efficiency among studies catalysts [25, 26]. Debe et al. developed nanostructured thin films (NSTF) by sputtering Pt–Ir nanoparticles onto organic whisker arrays and evaluated its OER activity which achieved a current density of 2 A cm^{-2} at 1.81 V with a Ir loading of 0.3 mg cm^{-2} at the anode [27]. Despite these advances, the Ir and Pt usage and the longevity of these catalysts are still far from the requirements for the commercialization of PEMWE [10], and they have yet to be tested in a real practical PEMWE cell. Moreover, the use of Pt–Ir catalysts for both the anode and cathode in PEMWE remains underexplored.

The choice of supporting material is critical for achieving high catalytic activity and durability. Supports with high surface area and appropriate porosity can enhance the dispersion of Pt–Ir nanoparticles, improve mass transfer, and mitigate particle agglomeration during operation. For instance, metal oxide-supported Ir oxides exhibit higher activity and durability than carbon-supported counterparts due to strong metal–support interactions (MSI), which tune the electronic configuration of Ir and mitigate over-oxidation and dissolution during OER [28]. Metal–organic frameworks (MOFs) and their derivatives, with their inherently high BET surface area and porosity, demonstrated advantages in mass transfer

 https://doi.org/10.1007/s40820-025-01845-7

during OER [29, 30]. Transition metal oxides, such as Co_3O_4 and MoO_3, have shown promise as bifunctional catalysts due to their redox efficiency, tunable electronic properties, and structural flexibility [31–33]. Particularly, Co-based species have demonstrated high activity and long-term durability toward OER in both acidic and alkaline media [34–37]. For example, oxovanadate-doped cobalt carbonate on nickel foam ($VCoCO_x$@NF) exhibited high overall water splitting performance, including both HER and OER, in an alkaline anion-exchange membrane water electrolyzer (AAEMWE) [34]. Spinel-structured Co_3O_4 demonstrated remarkable stability in acidic environments compared to other cobalt-based materials (e.g., CoSe, CoP, CoB, and CoO) [38]. Doping with elements such as lanthanum (La) and manganese (Mn) can further enhance catalytic activity, durability, and electronic conductivity [39]. Hierarchical porous Co_3O_4 microtube arrays have also demonstrated excellent bifunctional activity and stability for both OER and HER [32]. The affinity between Co and Pt [40] and between Co and Ir [41] suggests that transition metal-doped Co_3O_4 could serve as an effective support for Pt–Ir nanoparticles. Such supports not only provide anchoring sites for nanoparticles but also enable metal/metal oxide support interactions (MMOSI), stabilizing the nanoparticles and enhancing their catalytic performance [28]. Motivated by these findings, we report a bifunctional catalyst design: an iridium–platinum subnanoalloy (IrPt) supported on lanthanum and nickel co-doped cobalt oxide (La–Ni–Co_3O_4). This catalyst features a unique core–shell structure, comprising an amorphous $IrPtO_x$ shell and an IrPt core, which synergistically enhances both OER and HER activities while addressing the critical challenges of PGM usage and durability in PEMWE. Unlike our previous studies [29], the introduction of Ni in this work introduces additional defect sites and optimizes the electronic structure of the support, leading to improved performance. Central to the catalyst's performance is its unique core–shell structure, where the amorphous $IrPtO_x$ shell and IrPt core work synergistically to enhance catalytic activity and stability. The amorphous IrPtOx shell provides abundant active sites and facilitates charge transfer, while the IrPt core ensures structural integrity and electronic conductivity. This dual-phase architecture not only optimizes the adsorption energies of reaction intermediates but also mitigates the dissolution and agglomeration of active sites during prolonged operation, addressing a key limitation of traditional PGM-based catalysts.

The Ir–Ir/Pt bond distance in the resulting catalyst (IrPtOx-S, S is the support) (~2.75 Å) is shorter than that in IrO_2 (~3.22 Å), enabling a bi-nuclear OER mechanism where two adjacent $*=O$ intermediates directly couple to form O_2 [42]. This pathway bypasses lattice oxygen participation and avoids high-energy intermediates like $*OOH$, relying solely on $*O$ and $*OH$ as reaction intermediates. By circumventing the scaling relationship limitations of the adsorbate evolution mechanism (AEM) and eliminating metal leaching risks inherent to the lattice oxygen mechanism (LOM) [43], this approach offers enhanced stability. The bi-nuclear mechanism requires precise geometric alignment of active sites (typically 2.4–2.9 Å) [44], a criterion satisfied by the optimized Ir–Pt coordination in our $IrPtO_x$-S. For HER in acidic media, the process initiates with the Volmer step ($H^+ + e^- \rightarrow H$), forming adsorbed hydrogen (H*) on the catalyst surface. The reaction then proceeds via either the Heyrovsky step ($H^* + H^+ + e^- \rightarrow H_2$) or the Tafel step ($2H^* \rightarrow H_2^*$). For highly active HER catalysts (e.g., Pt-based systems), the Volmer–Tafel pathway dominates, characterized by Tafel slopes ≤ 29 mV dec^{-1} [45]—a benchmark met by our $IrPtO_x$-S catalyst (26 mV dec^{-1}). Our IrPtOx-S exhibited exceptional OER and HER activity, with mass activities of 1188.0 ± 30 A g_{Ir}^{-1} at 300 mV overpotential for OER and 8725 ± 70 A g_{Pt}^{-1} at 100 mV overpotential for HER in 0.1 M $HClO_4$, representing 33.3-fold and 8.2-fold improvements over commercial IrO_2 and Pt/C benchmarks, respectively. The catalyst also demonstrated remarkable durability, sustaining OER at 10 mA cm^{-2} and HER at -10 mA cm^{-2} in acidic media for over 1000 h, respectively. When integrated into a membrane electrode assembly (MEA) as both the anode and cathode, the PEMWE cell achieved a current density of 2 A cm^{-2} at 1.72 V with ultralow loadings of 0.075 mg_{Ir} cm^{-2} Ir at the anode and 0.075 mg_{Pt} cm^{-2} Pt at the cathode. To elucidate the underlying mechanisms, we employed density functional theory (DFT) calculations combined with in situ X-ray absorption spectroscopy (XAS) to systematically investigate the catalytic reaction pathways and the origins of the catalyst's high activity and stability under PEMWE conditions.

2 Experimental Section

2.1 Preparation of the Support Material

6 g of $Co(NO_3)_2 \cdot 6H_2O$, 1.81 g of $La(NO_3)_3 \cdot xH_2O$, and 2.02 g of $Ni(NO_3)_2 \cdot 6H_2O$ were dissolved in 150 mL of methanol

to form Solution A. Separately, 15 g of 2-methylimidazole was dissolved in 400 mL of methanol to prepare Solution B. Solution A was added dropwise to solution B under continuous stirring at room temperature until a uniform mixture was obtained. The mixture was then sealed and kept at room temperature for 8 h. The resulting La- and Ni-doped Co-MOF was collected by centrifugation, washed three times with methanol, and dried under vacuum overnight. The La-Ni co-doped Co-MOF was carbonized in a tube furnace at 510 °C for 1 h under an argon atmosphere. The carbonized powder was further annealed at 360 °C in air for 4 h to yield the porous support material, La-Ni co-doped Co_3O_4 (denoted as S).

2.2 Preparation of IrPtOx-S, IrOx-S, and Pt–S

38.09 mg of $IrCl_3 \cdot nH_2O$, 43.5 mg of $C_{10}H_{14}O_4Pt$, 2.7 g of 1,4-phthalaldehyde, and 1.54 g of citric acid were mixed with 64.8 mL of benzyl alcohol and ultrasonicated for 1 h. Subsequently, 140 mg of the support material (S) was added to the mixture and ultrasonicated until a uniform dispersion was achieved. The mixture was then heated at 190 °C for 4 h in an oil bath. After natural cooling, the product was centrifuged, washed three times with a mixture of acetone and ethanol, and freeze-dried in liquid nitrogen. Finally, the material was annealed at 360 °C for 4 h under flowing air to obtain $IrPtO_x$-S. The preparation methods for IrOx-S and Pt–S were the same as that for $IrPtO_x$-S, except for the absence of $C_{10}H_{14}O_4Pt$ or $IrCl_3 \cdot nH_2O$ during the solvothermal reduction step.

2.3 Characterization

The microstructure and morphology of the materials were characterized using spherical aberration-corrected transmission electron microscope (AC-TEM), high-resolution TEM (HRTEM), and high-angle annular dark field-scanning TEM (HAADF-STEM). These analyses were performed on a Talos F200X G2 microscope and a JEOL ARM-200F electron microscope equipped with a spherical aberration corrector (CEOS GmbH), both operated at 200 kV. Energy-dispersive X-ray spectroscopy (EDS) was performed on the same instrument at 200 kV. Powder X-ray diffraction (XRD) patterns were collected using a Mini Flex 600 diffractometer with Cu Kα radiation ($\lambda = 1.5406$ Å) over a 2θ range of 5° to 90°. The surface chemical valence states were analyzed using X-ray photoelectron spectroscopy (XPS) on an AXIS UltraDLD spectrometer with a monochromatic Al Kα source. The binding energies were calibrated using the C 1 *s* peak at 284.8 eV to account for charging effects. Raman spectroscopy was performed using a Renishaw inVia Qontor system with a 532 nm laser to analyze chemical bonding. The concentrations of Ir and Pt were determined using inductively coupled plasma mass spectrometry (ICP-MS, Nex ION 2000). The specific surface area and pore size distribution were analyzed using the Brunauer–Emmett–Teller (BET) method via nitrogen adsorption–desorption at 77 K on an Autosorb-iQ3 surface characterization analyzer.

2.4 Ex-Situ and In-Situ X-Ray Absorption Measurements

X-ray absorption spectra (XAS) were collected at two beamlines: BL14W1 at the Shanghai Synchrotron Radiation Facility (SSRF, China) using a Si (111) double-crystal monochromator, and the Optique Dispersive EXAFS (ODE) line station at the SOLEIL Synchrotron (France). The energy was set to 11,215 eV for the Ir L_{III} edge, 11,564 eV for the Pt L_{III} edge, and 7709 eV for the Co K edge. Spectra were collected at room temperature in fluorescence mode at BL14W1 and in transmission mode at ODE. Reference materials, including commercial IrO_2, Ir black, IrO_2/NbOx, Pt/C, $PtO_2 \cdot xH_2O$, Co_3O_4, and CoO, were measured for comparison. XAS data were processed and analyzed using Athena and Artemis software following standard procedures. Wavelet transform–extended X-ray absorption fine structure (WT-EXAFS) for k^2-weighted EXAFS oscillations enables the identification of bond pair contributions to the Fourier transform peaks. For in situ XAS measurements, a custom-designed electrochemical cell was used. The working electrode (WE) consisted of a catalyst-modified graphene sheet, while a Pt wire and Hg/Hg_2SO_4 served as the counter electrode (CE) and reference electrode (RE), respectively. The electrolytes were O_2-saturated 0.1 M $HClO_4$ for OER and H_2-saturated 0.5 M H_2SO_4 for HER. Additionally, X-ray absorption near-edge structure (XANES) spectra at the O K-edge were collected in total electron yield (TEY) mode using soft X-ray absorption spectroscopy at the BL08U1-A beamline of SSRF, with the absorption energy set at 543.1 eV.

 https://doi.org/10.1007/s40820-025-01845-7

2.5 Electrochemical Characterization

The electrochemical performance of the catalysts was evaluated using a standard three-electrode system with an electrochemical workstation (WaveDriver200, Pine, PHYCHEMI). For OER measurements, the electrolyte was O_2-saturated 0.1 M $HClO_4$, the WE was a catalyst-coated gold disk electrode (GDE, 5.0 mm diameter, Pine, PHYCHEMI), the CE was a gold wire, and the RE was Hg/Hg_2SO_4 (Pine Instruments).The catalyst ink was prepared by ultrasonically dispersing 2 mg of catalyst in a mixture of 0.4 mL deionized water, 0.3 mL isopropanol, and 3 μL 5% Nafion. 10 μL of the ink was drop-cast onto the gold disk, with an Ir loading of 10 μg cm^{-2}. For the support material (S), the loading was 150 μg cm^{-2}, and for commercial IrO_2, the Ir loading was 44 μg cm^{-2}.

For HER measurements, the electrolyte was H_2-saturated 0.1 M $HClO_4$ and 0.5 M H_2SO_4 solution, respectively. WE was a catalyst-coated glassy carbon disk electrode (GDE, 5.0 mm diameter, Pine Instruments), the CE was a graphite electrode, and RE was Hg/Hg_2SO_4 (Pine Instruments) The catalyst ink was prepared by ultrasonically dispersing 2 mg of catalyst and 0.2 mg of carbon in a mixture of 0.4 mL deionized water, 0.3 mL IPA, and 0.003 mL 5% Nafion. 10 μL of the ink was drop-cast onto the glassy carbon disk, with a Pt loading of 0.010 mg cm^{-2}. For commercial Pt/C, the Pt loading was also 0.020 mg cm^{-2}. All potentials were referenced to the reversible hydrogen electrode (RHE).

For OER testing, linear sweep voltammetry (LSV) was performed in O_2-saturated 0.1 M $HClO_4$ from 1.0 to 2.0 V (vs. RHE) at a scan rate of 2 mV s^{-1} with 85% iR compensation. For HER testing, LSV was performed in H_2-saturated 0.1 M $HClO_4$ from 0 to − 0.5 V (vs. RHE) at a scan rate of 2 mV s^{-1} with 85% iR compensation. Before LSV, the catalysts were stabilized by multiple cyclic voltammetry (CV) cycles at 100 mV s^{-1}. Each sample was tested at least three times for reproducibility.

OER overpotential (η_{OER}) was calculated at 10 mA cm^{-2} using $\eta_{OER} = E_{RHE} - 1.23$ V. HER overpotential (η_{HER}) was calculated at − 10 mA cm^{-2} using $\eta_{HER} = E_{RHE} - 0$ V. The Tafel slope was determined from the Tafel equation, $\eta = b \log j + a$, where b is the Tafel slope and j is the current density. The electrochemical surface areas (ECSAs) of the samples in units of $m^2\ g^{-1}$ were calculated using the equation: $ECSA = Q/(r.L)$, where Q is the integrated charge density (C cm^{-2}), Γ is the specific charge required to oxidize/reduce a monolayer of the adsorbed species (210 μC cm^{-2} for Pt, 596 μC cm^{-2} for IrO_2) [46], and L is the Pt or Ir loading of the electrode (g m^{-2}). Hydrogen underpotential deposition (H-UPD) method was used for $IrPtO_x$-S, Pt–S, and Com. Pt/C. Redox-active surface charge method was used for IrO_x-S and Com. IrO_2. The turnover frequency (TOF) was calculated based on equation: $TOF = j \times A/(4 \times F \times n)$, where j is the current density, A is the electrode area, F is the Faraday constant (96,485 C mol^{-1}), and n is the number of Ir or Pt atoms participating in the reaction (obtained from ECSA). The accelerated stress test (AST) for OER was performed in O_2-saturated 0.1 M $HClO_4$ from 1.3 to 1.8 V (vs. RHE) at 100 mV s^{-1} for 40,000 cycles. The AST for HER was performed in H_2-saturated 0.5 M H_2SO_4 from 0 to − 0.8 V (vs. RHE) at 100 mV s^{-1} for 40,000 cycles. LSV polarization curves were recorded before and after AST. Chronoamperometric measurements were conducted at constant current density of ± 10 mA cm^{-2} for OER and HER, respectively. The electrolytes were refreshed periodically.

2.6 PEMWE Performance Measurements

PEMWE cell performance was evaluated using a 600 ETS instrument (Scribner). Membrane electrode assemblies (MEAs) were prepared using the catalyst-coated membrane (CCM) method with GORE membranes (GORE-SELECT® M275.80, W. L. Gore & Associates, proton resistance of 57 mΩ cm^2 at 80 °C and 100% relative humidity), Ti felt (STi025-Pt0.5) as anodic gas diffusion layer (GDL), and carbon paper (Toray, TGP-H-060) as cathodic GDL. For reproducibility, at least three MEAs were assembled and tested for each sample. For MEA fabrication, the ink was prepared by ultrasonically dispersing the catalyst, 5 wt% Nafion ionomer, IPA, and deionized water, followed by spraying onto the membrane. The active geometric area of the MEA is 5 cm^2. For MEAs with IrPtOx-S as the anode, cathode, or both, Ir loadings were set at 0.075 mg cm^{-2} at anode, and Pt loadings were set at 0.075 mg cm^{-2} at cathode, respectively. For MEAs with IrO_2/NbO_2 (anode, Umicro) and Pt/C (cathode, TKK), the Ir loadings were set at 0.2 mg cm^{-2}, and Pt loadings were set at 0.3 mg cm^{-2}, respectively. Polarization curves were recorded at a scan rate of 0.008 A min^{-1} from 0 to 20 A at 80 °C. The long-term durability measurements of MEAs were conducted at constant current density of 1.8 A cm^{-2}.

2.7 ICP-MS Measurements and Lifetime Estimation

The composition of the catalyst and the dissolved metal ions were analyzed using an inductively coupled plasma mass spectrometer (ICP-MS, Agilent 7900). Prior to measurements, the ICP-MS instrument was calibrated by using multi-element solutions containing Ir, Pt, Co, and La with concentrations of 0.2, 1, 5, 20, and 200 ppb, respectively. To measure the dissolved metals during durability tests at a constant current density of 10 mA cm^{-2}, the electrolytes were replaced after each collection for subsequent ICP-MS analysis. At every interval, a portion of the electrolyte was collected, and the leached metal elements were quantitatively measured. The average dissolution rate of the leached elements was calculated using the following equation:

$$v = \frac{V \cdot C_{ICP}}{t \cdot m \cdot \mathrm{wt\%}} \quad (1)$$

where V is the volume of the electrolyte, C_{ICP} is the concentration of elements leached into the electrolyte, t is the time interval between two electrolyte collections, m is the total weight of the electrode, and wt% is the weight percentage of the leached element in the catalyst.

The stability number (S1) was determined by the following equation [47]:

$$S1 = \frac{n_{\mathrm{Oxygen(OER)}}}{n_{\mathrm{Ir(dissolved)}}} \quad (2)$$

The catalyst lifetime was estimated using the equation [47]:

$$t_{\mathrm{lifetime}} = \frac{S \cdot Z \cdot F \cdot m}{j \cdot M} \quad (3)$$

where $t_{lifetime}$ is the lifetime of the catalyst, S is the stability number, Z is the number of electrons per evolved O_2, F is the faraday constant, m is the loaded mass of Ir or Pt (g cm^{-2}), j is the applied current density (A cm^{-2}), and M is the molar mass of Ir or Pt.

2.8 ^{18}O MS Test

A working electrode was prepared by drop-casting the catalyst ink onto a glassy carbon electrode (GDE). The ink was prepared by dispersing 6 mg of catalyst powder in a mixture of 31 μL Nafion and 2 mL isopropanol, followed by ultrasonication for 30 min. Electrochemical measurements were performed using an Autolab electrochemical workstation in a three-electrode cell, consisting of the catalyst-modified working electrode, an Hg/Hg_2SO_4 reference electrode, and a Pt wire counter electrode. To label the catalyst with ^{18}O, the working electrode was first operated at a constant current density of 15 mA cm^{-2} for 10 min in 0.1 M $HClO_4$ electrolyte prepared with $H_2{}^{18}O$ (Sinopharm Chemical Reagent Co., Ltd). The electrode and cell were then rinsed with deionized water to remove any residual $H_2{}^{18}O$. Subsequently, the electrode was operated at 15 mA cm^{-2} for an additional 30 min, during which mass-selected product signals ($m/z = 32$ and 34) were collected every 5 min using a GC–MS system with an ionization voltage of 70 eV. Each data point represents the average of five measurements, and all results were background-subtracted.

2.9 DFT Calculations

Periodic density functional theory (DFT) calculations were performed using the projected augmented wave (PAW) method implemented in the Vienna Ab-initio Simulation Package (VASP) [48]. The calculations employed the Perdew–Burke–Ernzerhof (PBE) exchange–correlation functional within the generalized gradient approximation (GGA), supplemented with van der Waals (vdW) corrections [49, 50]. A set of $3 \times 6 \times 1$ and $6 \times 9 \times 1$ Monkhorst–Pack grids were used for geometric optimization, with a cutoff energy of 400 eV for plane-wave basis setup. The maximum atomic forces and energy were ≤ 0.01 eV $Å^{-1}$ and 10^{-5} eV $cell^{-1}$, respectively. For the slab model, a 15 Å vacuum layer was added along the z-axis to prevent interactions between periodic images. To account for the strong on-site Coulomb repulsion among transition metals, the GGA + U approach was employed by introducing a Hubbard-like repulsion term (Ueff = U–J) [51]. The Ueff value for Co was set to 3.3 eV.

The reaction mechanism was evaluated using a three-state diagram, including an initial state (H^+), an intermediate state (H*), and the final product (½ H_2). For the oxygen evolution reaction (OER), the intermediates included OH*, O*, and OOH*. Based on in situ XANES results, projected density of states (pDOS) analysis, and TEM images, an Ir–O–Pt model was used to simulate the active sites for OER and HER.

The free energy of adsorption ($\Delta G_{\mathrm{adsorbate}}$*) was used as a descriptor to evaluate catalytic activity. The free energies of intermediates at 298 K were calculated using the equation:

$$\Delta G_{\mathrm{adsorbate}*} = \Delta E_{\mathrm{adsorbate}*} + \Delta E_{\mathrm{ZPE}} - T\Delta S_{\mathrm{H}} + eU \quad (4)$$

https://doi.org/10.1007/s40820-025-01845-7

where $\Delta E_{adsorbate*}$ is the binding energy of the absorbed intermediates, ΔE_{ZPE} is the zero-point energy changes, $T\Delta S_H$ is the entropy at room temperature ($T = 298.15$ K), and eU is the applied potential. The limiting potential (U_L) and overpotential (η) were determined using:

$$U_L = \Delta G_{max}/ne \quad (5)$$

$$\eta = U_{ideal} - U_L \quad (6)$$

where ΔG_{max} is the free energy change of the rate-determining step (RDS), n and e are the number of electrons and electron charge [52], respectively. U_{ideal} is the theoretical potential from a thermodynamic perspective.

3 Results and Discussion

3.1 Synthesis and Characterization of $IrPtO_x$-S

IrPtOx-S was synthesized through a solvothermal method, involving the in situ reduction of Pt and Ir on the surface of a carbonized La- and Ni-doped cobalt metal–organic framework, followed by calcination in flowing air at 360 °C. During the calcination in flowing air, the carbon template was completely removed, leaving a highly porous and conductive oxide support. A schematic of the synthesis process is shown in Fig. 1a.

XRD analysis confirmed the formation of an Ir–Pt alloy and spinel-structured Co_3O_4 (Fig. 1b). The peaks corresponding Ir–Pt were shifted to higher angles (Fig. 1b, inset), indicating compressive strain in the Ir–Pt particles. Such lattice strain is known to enhance catalytic activity by optimizing the adsorption energy of intermediates [53]. Raman spectroscopy revealed lattice expansion induced by transition metal doping, as evidenced by red-shifted Raman bands and broadened peaks compared to pure Co_3O_4 (Fig. 1c). A broad peak in the 549–625 cm^{-1} range was attributed to amorphous IrOx [54], suggesting the surface of Pt–Ir alloy may be covered by amorphous Ir-O phases. These structural modifications are critical for improving the catalyst's electronic properties and reactivity.

The catalyst was highly porous, as indicated by scanning electron microscopy (SEM) (Fig. S1). TEM images (Fig. 1d) clearly distinguished individual transition metal dopants, e.g., La, Ir, and Pt uniformly dispersed within the Co_3O_4 lattice, as heavier atoms appeared brighter due to their higher atomic numbers [55]. The average particle sizes of IrPt alloy and the whole catalyst, determined by measuring hundreds of particles across different regions, were estimated to be 2.1 and 3.0 nm, respectively (Figs. 1e and S2), highlighting the nanoscale nature of the catalyst. HR-TEM images revealed the surface of IrPt alloy being covered by an amorphous species with thickness of ~ 2 nm, which can be ascribed to the amorphous IrOx/$IrPtO_x$ based on Raman result (Fig. 1f). Amorphous IrO_x is known to possess abundant metal dangling bonds and flexible unsaturated electronic configurations, which enhance orbital coupling with intermediates, facilitate charge transfer, and improve catalytic activity [56]. The lattice spacings of 2.3 and 2.5 Å were assigned to the Ir–Pt (111) and Co_3O_4 (311) planes, respectively (Figs. 1f, h and S3). The Ir–Pt (111) spacing was smaller than that of pure Ir–Pt (111) (2.4 Å) [57], suggesting ~ 4% lattice compression, consistent with the XRD results. Conversely, the Co_3O_4 (311) spacing was expanded compared to pure Co_3O_4 (311) (2.4 Å) [58], indicating successful doping of transition metals into the Co_3O_4 lattice. These lattice strain and defects induced by doping optimize the adsorption energy of active sites for intermediates, enhancing catalytic activity [53]. Additionally, the size and oxidation state differences among different dopants create lattice distortions, which mitigate element dissolution during corrosive catalytic processes [59]. Lattice expansion and disordered edges, induced by interactions between components of different sizes, were clearly visualized (Fig. 1h). These features modify the d-band and electronic structures of active sites, improving catalytic activity and mass transfer [56]. Elemental mapping confirmed the uniform distribution of Co, O, La, Ni, Ir, and Pt throughout the catalyst (Figs. 1I and S4–S5) and supported the formation of Ir–Pt alloy nanoparticles (Fig. 1I, Ir and Pt images). STEM-EDS line-scan profiles further confirmed the formation of IrPt alloy core with particle size being around 2–3 nm and IrPtOx shell with thickness of 2–3 nm (Fig. S4b). The concentrations of Ir and Pt were quantified to be 6.738 and 6.779 wt% by ICP-MS (Table S1). N_2 adsorption–desorption analysis revealed a BET surface area of 144.5 $m^2\ g^{-1}$ and an average pore diameter of 5.5 nm (Fig. S6, Table S2). The hierarchical porosity and high surface area of the catalyst facilitate mass transport and expose abundant active sites, further enhancing its performance.

XPS was employed to investigate the surface structure and oxidation states of each element in the catalyst. The

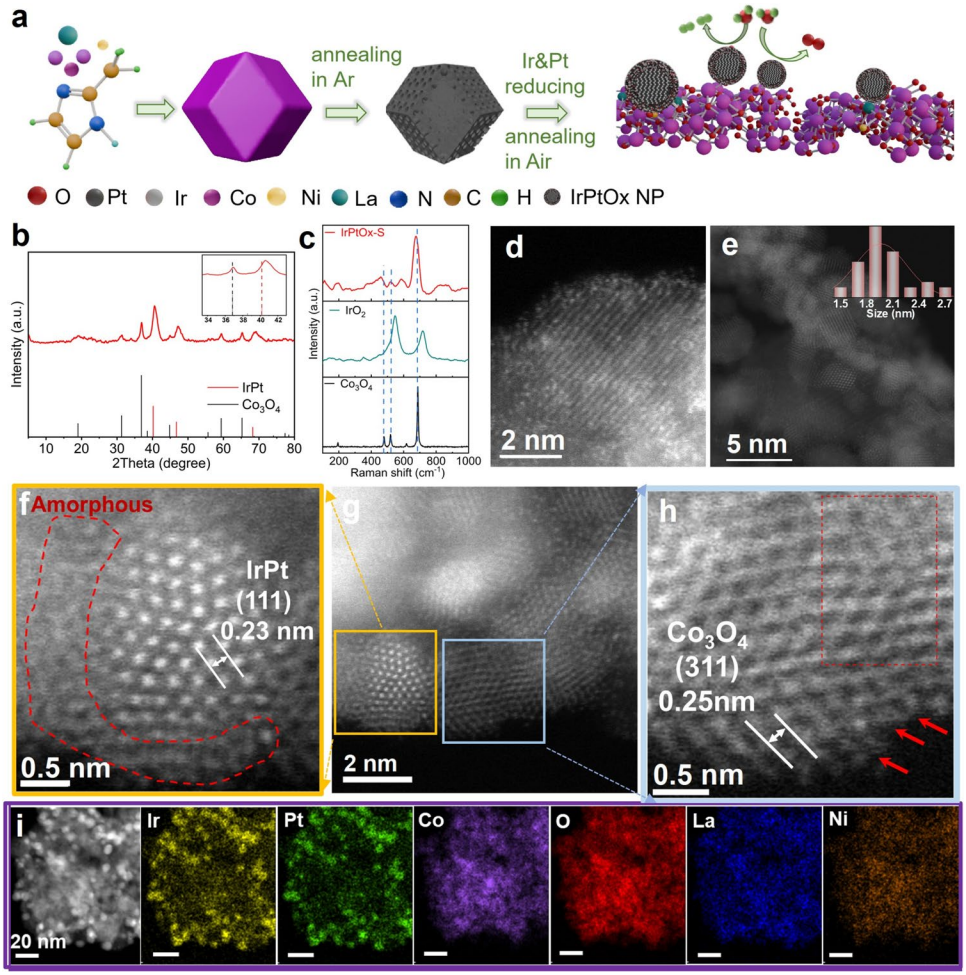

Fig. 1 Structure characterizations of IrPtOx-S: **a** illustration of IrPtOx-S synthesis. **b** XRD pattern. **c** Raman spectrum. IrO_2 and Co_3O_4 were the references. **d** AC-TEM image of support material (S). **e** Particle size distribution of IrPt. **f**, **h** HRTEM images of individual particles indicated in g). **g** HRTEM image of IrPtOx-S. **i** HAADF-STEM and corresponding elemental mapping images of Ir, Pt, Co, La, Ni, and O

survey spectrum confirmed the presence of Co, La, Ni, Pt, Ir, and O (Fig. S7a). The Ir 4*f* spectrum was deconvoluted into three sets of doublets: 60.8/63.8 eV (Ir^0), 61.8/63.6 eV (Ir^{4+}), and 62.4/65.3 eV (Ir^{3+}) (Fig. 2a) with the Ir^0 as the dominate [60]. The presence of Ir^0 supports the formation of a Pt–Ir alloy, while the presence of Ir^{3+} and Ir^{4+} suggests the coexistence of amorphous Ir-O phase on the metal surface, in line with XRD and Raman results. The Pt 4*f* spectrum featured four peaks: 71.4 eV (Pt^0 $4f_{7/2}$), 74.7 eV (Pt^0 $4f_{5/2}$), 72.16 eV (Pt^{2+} $4f_{7/2}$), and 75.78 eV (Pt^{2+} $4f_{5/2}$) with Pt^0 as the dominate [61] (Fig. 2b). XPS results further suggest that the surface of the IrPt alloy is covered by Ir–Pt–O phase. Compared to IrO_x-S and Com. IrO_2, the binding energy of Ir 4*f* in $IrPtO_x$-S indicates that the introduction of Pt mitigates Ir oxidation during annealing, favoring Pt–Ir alloy formation (Fig. S8a). The Pt^0 4*f* binding energy in $IrPtO_x$-S was positively shifted by 0.3 eV relative to pure Pt^0, indicating electron redistribution between Pt and Ir due to their differing electronegativities (Fig. S8b).

The O 1*s* spectrum was deconvoluted into three peaks: 530.1 eV (lattice oxygen), 531.4 eV (oxygen vacancies, V_o), and 533.3 eV (surface hydroxyl groups) [62] (Fig. 2c). The high concentration of oxygen vacancies was further confirmed by electron paramagnetic resonance (EPR) spectroscopy, which showed a stronger signal at g = 2.003 compared to that of catalyst without Pt (IrO_x-S) [63, 64] (Fig. 2d). The introduction of Pt significantly increased the oxygen vacancy concentration, driven by charge compensation

 https://doi.org/10.1007/s40820-025-01845-7

effects as lower-valent Pt substitutes for higher-valent Ir/Co. This substitution necessitates the removal of oxygen atoms to maintain charge neutrality, creating a highly active and conductive catalyst surface. These observations strongly support the idea that the coexistence of multiple elements (La, Ni, Co, Pt, and Ir) induces a redistribution of electronic coupling among the metal ions, enhancing the material's catalytic properties. Additionally, oxygen vacancies enhance electron conductivity and catalytic activity by facilitating electron transfer [65]. The Co 2*p* spectrum exhibited characteristic peaks of spinel-structured Co_3O_4, with Co^{3+} $2p_{3/2}$ at 779.8 eV, Co^{2+} $2p_{3/2}$ at 781.0 eV, and a Co^{2+} satellite peak at 785.8 eV [66] (Fig. S7b). The Co^{3+}/Co^{2+} ratio in the catalyst was lower than that of pure Co_3O_4, suggesting partial substitution of Co^{3+} by dopants such as Ir^{3+}, La^{3+}, or Ni^{3+}. XPS spectra also revealed that La was partially attached to hydroxyl groups (Fig. S7c). It is well-known that hydroxyl groups on the surface of nanomaterials can enhance pseudocapacitance, thereby exposing more accessible active sites and boosting catalytic activity [47].

XAS spectra including XANES and EXAFS were performed at Ir L_{III}, Pt L_{III}, and Co K edges to investigate the electronic structure and local atomic environment of IrPtOx-S. The XANES spectrum at Ir L_{III} edge reflects the unoccupied 5*d* states, where the peak position shifts to higher energies and the integrated intensity of the white line increases with the number of *d* holes (*d* vacancies) [60]. Figure 3a shows the XANES spectrum at the Ir L_{III} edge for $IrPtO_x$-S, along with references for $IrCl_3$, IrO_2, and Ir foil. The absorption energy of Ir L_{III} edge in $IrPtO_x$-S is close to that of Ir foil, but the white line peak is shifted by 1.5 eV to higher energy, positioned between $IrCl_3$ and IrO_2 (inset of Fig. 3a). This indicates that Ir in $IrPtO_x$-S exists in a mixed oxidation state ranging from 0 to +4.

The EXAFS spectrum at the Ir L_{III} edge shows two distinct peaks in R space (Fig. 3b). The first peak at 2.30 is 0.23 Å shorter than the Ir–Ir bond in Ir foil (2.53 Å), suggesting the formation of an Ir–Pt bond and IrPt alloy. The shorter Ir–Pt bond distance may be attributed to the compression of the Ir–Pt bond, as shown in XRD pattern. The second peak at 3.21 Å is assigned to Ir–O–Pt, distinguishable from the Ir–O–Ir bond (3.01 Å) in IrO_2. The longer bond distance of Ir–O–Pt compared to Ir–O–Ir may result from the amorphous portion of $IrPtO_x$ covering

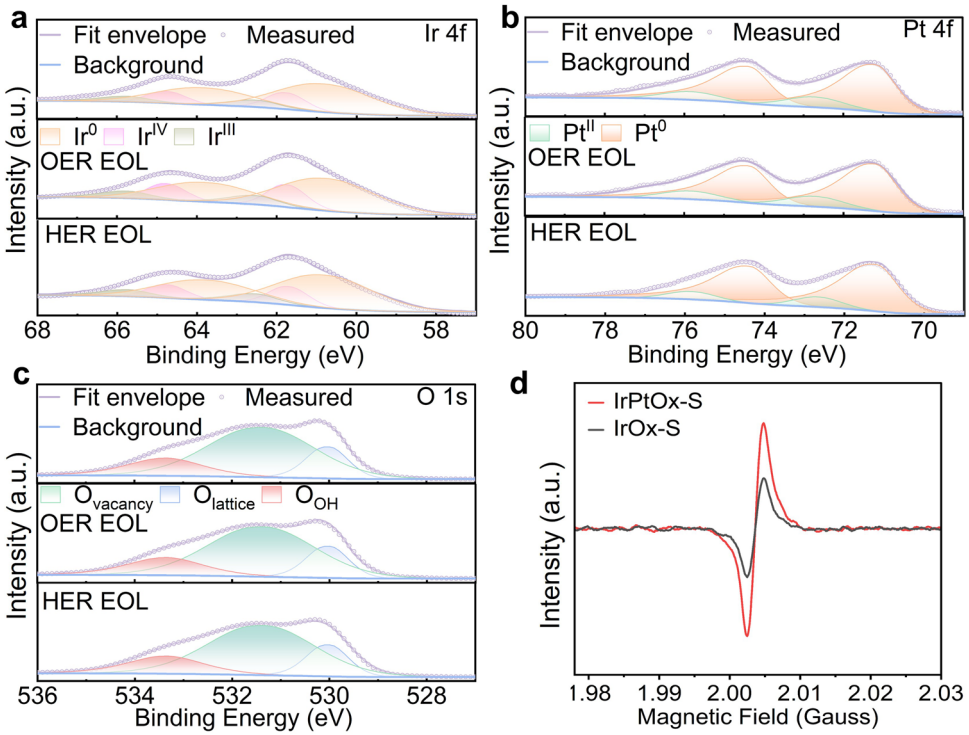

Fig. 2 Chemical and structural analysis of IrPtOx-S. XPS spectra of **a** Ir 4*f*, **b** Pt 4*f*, **c** O 1*s* of fresh sample (top), and the samples peeled off from the MEA at the end of life (EOL) test of OER (anode) and HER (cathode), respectively. **d** EPR spectra of IrPtOx-S and IrOx-S

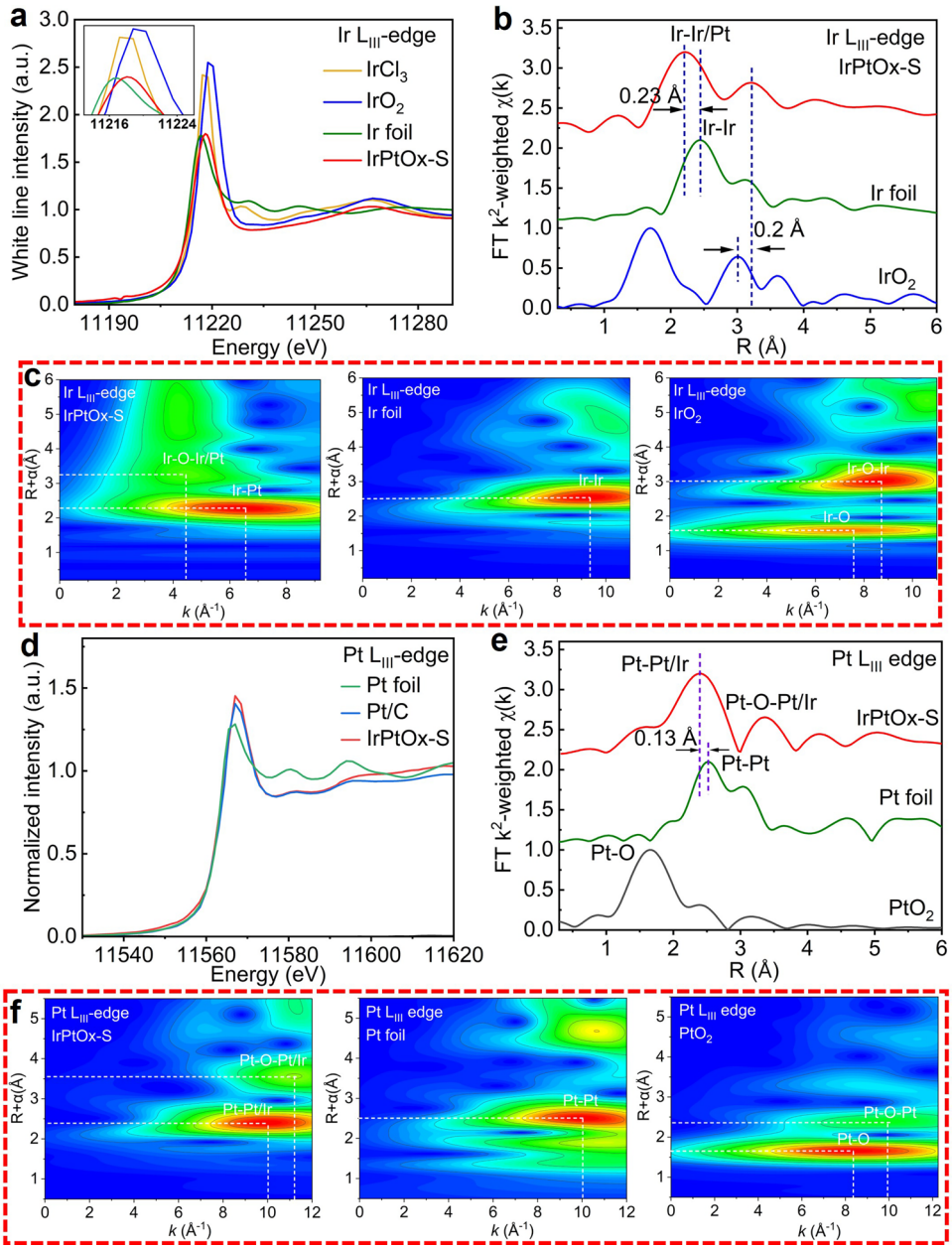

Fig. 3 Electronic and atomic structure analysis of IrPtOx-S. **a** XANES spectra, **b** k^2-weighted FT EXAFS spectra, and **c** wavelet transform images of Ir L_{III}-edge EXAFS. $IrCl_3$, IrO_2, and Ir foil were the references. **d** XANES spectra, **e** k^2-weighted FT EXAFS spectra, and **f** wavelet transform images of Pt L_{III}-edge EXAFS. Pt foil, Pt/C, and PtO_2 were the references

outside of the IrPt alloy. WT-EXAFS analysis further confirmed the differences between Ir–Pt and Ir–Ir, as well as between Ir–O–Pt and Ir–O–Ir (Fig. 3c). The WT-EXAFS at the Ir L_{III} edge exhibits two characteristic regions: a first shell domain for Ir–Pt scattering at R = 2.28 Å and K = 6.55 $Å^{-1}$ and the second shell domain for Ir–O–Pt scattering at R = 3.21 Å and K = 4.45 $Å^{-1}$. In contrast, Ir–Ir scattering in Ir foil occurs at R = 2.53 Å and K = 9.36 $Å^{-1}$, while Ir–O–Ir scattering in IrO_2 occurs at R = 3.01 Å and K = 8.72 $Å^{-1}$. The distinct K values confirm the formation of Ir–Pt bond and the long-range disordered Ir-O-Pt bonds in $IrPtO_x$-S. The XANES spectrum at the Pt L_{III} edge indicates a predominantly metallic Pt surface with slight oxidation (Fig. 3d). The EXAFS spectrum shows

https://doi.org/10.1007/s40820-025-01845-7

two distinct peaks at 2.38 and 3.33 Å, corresponding to Pt–Ir and Pt–O–Ir scattering, respectively (Fig. 3e). The WT-EXAFS analysis, as shown in Fig. 3f, reveals the first shell domain for Pt–Ir scattering at R = 2.38 Å and K = 9.99 $Å^{-1}$, distinct from Pt–Pt scattering in Pt foil (R = 2.51 Å, K = 10.03 $Å^{-1}$), and the second shell domain for Pt–O–Ir scattering at R = 3.33 Å and K = 11.22 $Å^{-1}$, distinguishable from scattering in Pt foil or PtO_2, confirming the different local atomic environment of Pt in IrPtOx-S from that of the references.

The Co K-edge XANES spectrum of IrPtOx-S resembles that of Co_3O_4 but with lower white line intensity, indicating reduced Co–O coordination due to doping-induced oxygen vacancies (Fig. S9a). The EXAFS spectrum exhibits Co_3O_4-like features but with lower peak intensity, consistent with the presence of oxygen vacancies (Fig. S9b). These findings align with XPS results, confirming the existence of oxygen vacancies, which facilitate electron transfer and improve catalytic activity [65]. The WT-EXAFS analysis at the Co K-edge confirms the different local atomic environment of Co in IrPtOx-S from that of pure Co_3O_4 (Fig. S10).

3.2 Electrochemical Performance of IrPtOx-S

The OER performance of IrPtOx-S was evaluated in O_2-saturated 0.1 M $HClO_4$ using a three-electrode cell. For comparison, support (S), Pt–S, IrO_x-S, and Com. IrO_2 were tested under the same conditions, with all potentials referenced to RHE. As anticipated, $IrPtO_x$-S demonstrated the highest catalytic activity among all tested materials (Fig. 4a). Notably, S outperformed Com. IrO_2 (with an Ir loading of 44 μg cm^{-2}), underscoring the effectiveness of the support. The introduction of Pt improved the reaction kinetics of Pt–S at high potentials, while Ir significantly enhanced the OER activity of IrO_x-S, reducing the overpotential to reach 10 mA cm^{-2} from 360.3 mV for Pt–S (10 μg_{Pt} cm^{-2}) to 320.0 mV for IrOx-S (10 μg_{Ir} cm^{-2}). By forming an Ir–Pt alloy, $IrPtO_x$-S achieved an exceptionally low overpotential of 291.0 mV at 10 mA cm^{-2} with an ultralow Ir loading of 10 μg cm^{-2}, highlighting the synergistic effect of Pt in optimizing the electronic configuration of Ir for enhanced OER activity. The overpotentials at 10 mA cm^{-2} for all catalysts are summarized in Fig. 4b.

The exceptional activity of IrPtOx-S is further evidenced by its Tafel slope of 59 mV dec^{-1} (Fig. 4c), significantly lower than those of IrO_x-S (62 mV dec^{-1}), Pt–S (76 mV dec^{-1}), S (82 mV dec^{-1}), and Com. IrO_2 (87 mV dec^{-1}). This indicates improved electrocatalytic kinetics, which is attributed to the unique Ir–Pt alloy structure. The intrinsic catalytic activity was quantified using turnover frequency (TOF) and mass activity (MA) at 300 mV overpotential (Fig. 4d). The TOF of $IrPtO_x$-S was 1.00 ± 0.06 s^{-1}, 2.2 and 33 times higher than those of IrO_x-S (0.46 ± 0.05 s^{-1}) and Com. IrO_2 (0.03 ± 0.004 s^{-1}), respectively. Similarly, the MA of $IrPtO_x$-S reached 1188.0 ± 30 A g_{Ir}^{-1}, significantly surpassing those of IrO_x-S (648.0 ± 32 A g_{Ir}^{-1}) and Com. IrO_2 (35.7 ± 2 A g_{Ir}^{-1}), further underscoring its superior performance.

The long-term stability of $IrPtO_x$-S was evaluated via chronoamperometric (CA) at 10 mA cm^{-2} for 1020 h, demonstrating remarkable durability with only a 30 mV increase in potential (Fig. 4e). Gas chromatography (GC) confirmed the high purity of produced O_2 (> 99% faradaic efficiency, FE) throughout the test (Fig. 4e). ICP-MS revealed negligible dissolution of Ir, Pt, and Co during the CA test interval (Fig. 4f), highlighting the material's exceptional stability under harsh acidic conditions.

The S-number (a metric for catalyst stability [47]) and lifetime of $IrPtO_x$-S reached 1.42×10^7 n_{O2} n_{Ir}^{-1} and 1.43×10^8 h (Fig. 4g), respectively, surpassing most reported Ir- and Ru-based OER catalysts in acidic media (Fig. 4h, Table S3). Accelerated stress tests (AST) involving 40,000 cycles from 1.3 to 1.8 V further confirmed the superior stability of $IrPtO_x$-S compared to Com. IrO_2 (Fig. 4i), with only an 8 mV increase in potential at 10 mA cm^{-2} after the test. In contrast, the potential increased by 37 mV for Com. IrO_2 under the same conditions, underscoring the exceptional durability of $IrPtO_x$-S. These results collectively demonstrate the outstanding OER activity and stability of $IrPtO_x$-S in acidic media, positioning it as a leading candidate for practical PEMWE applications.

The HER performance of IrPtOx-S catalyst was evaluated in H_2-saturated 0.1 M $HClO_4$, with Pt–S, IrOx-S, S as control samples and Com. Pt/C as benchmark. Support (S) exhibited moderate HER activity, requiring an overpotential of 199.0 mV to reach − 10 mA cm^{-2}, comparable to non-precious metal catalysts [67]. The introduction of Pt and Ir significantly improved the HER activity, with Pt–S outperforming Com. Pt/C (Fig. 5a). Specifically, Pt–S

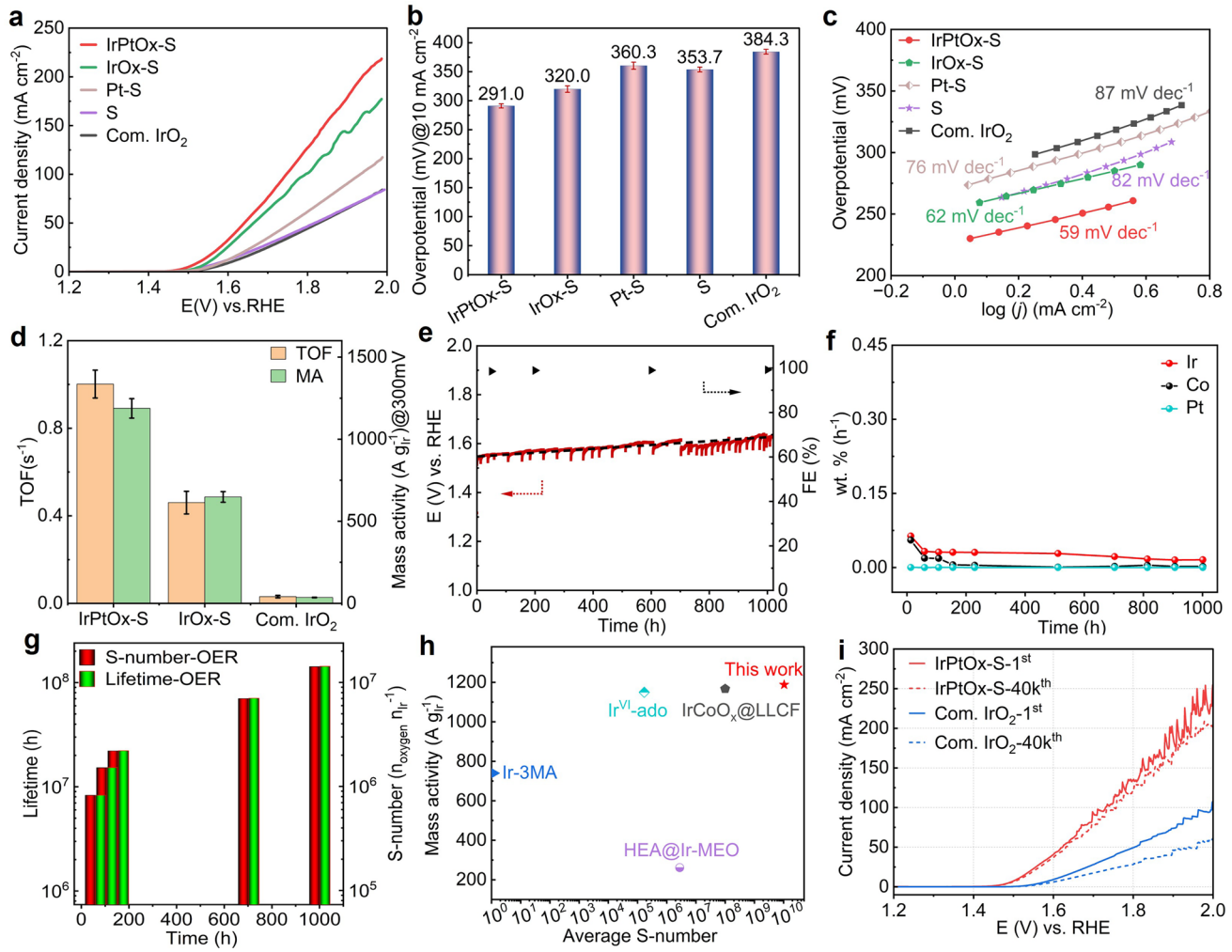

Fig. 4 Electrochemical OER of IrPtOx-S. **a** Polarization curves recorded on different samples using a three-electrode configuration in O_2-saturated 0.1 M $HClO_4$ electrolyte. Ir/Pt loading for IrPtOx-S, IrOx-S, and Pt–S was 10 $\mu g_{Ir/Pt}$ cm^{-2}, respectively. Ir loading for Com. IrO_2 was 44 ug_{Ir} cm^{-2}. The loading of support material (S) was 150 μg cm^{-2}. **b** overpotential at 10 mA cm^{-2} current density for different samples. **c** The relevant Tafel plots of the catalysts studied in (a). **d** Ir mass activities and TOF of different catalysts at an overpotential of 300 mV. **e** Chronoamperometric measurement on IrPtOx-S catalyst at 10 mA cm^{-2} current density for 1020 h in O_2-saturated 0.1 m $HClO_4$ electrolyte, and the FE as function of time. **f** The corresponding ICP-MS measurements and **g** S-number and lifetime calculation during chronoamperometric measurement shown in (**e**). **h** Comparison of S-number and Ir mass activity of IrPtOx-S to those of reported Ir-based OER catalysts. **i** Polarization curves of IrPtOx-S before and after 40,000 CV cycles from 1.3 to 1.8 V vs. RHE in O_2-saturated 0.1 m $HClO_4$ electrolyte. Com. IrO_2 was the benchmark

achieved − 10 mA cm^{-2} at overpotential of 72.7 mV with a Pt loading of 10 μg_{Pt} cm^{-2}, while 77.3 mV was required for Pt/C to reach the same current density with a higher Pt loading of 20 μg cm^{-2} Pt. The $IrPtO_x$-S catalyst demonstrated the highest HER activity, achieving − 10 mA cm^{-2} at overpotential of 60.0 mV and delivering a current density of 400 mA cm^{-2} at − 0.24 V, 2.6 and 3.7 times higher than that produced by Pt–S (− 153.7 mA cm^{-2}) and Pt/C (− 108.7 mA cm^{-2}) at the same potential (Fig. 5a). The overpotential at −10 mA cm^{-2} of different samples is summarized in Fig. 5b. The Tafel slope of $IrPtO_x$-S catalyst was 26 mV dec^{-1}, lower than those of Pt–S (36 mV dec^{-1}), IrO_x-S (115 mV dec^{-1}), and Pt/C (39 mV dec^{-1}) (Fig. 5c), indicating faster HER kinetics and a Tafel reaction pathway [45]. The TOF and MA of the $IrPtO_x$-S catalyst at 100 mV overpotential were 6.85 ± 0.23 s^{-1} and 8725.0 ± 70 A g_{Pt}^{-1}, respectively, 2.1&2.6 and 2.5&8.2 times higher than those of Pt–S (3.23 ± 0.16 s^{-1}, 3262.0 ± 50 A g_{Pt}^{-1}) and Pt/C

https://doi.org/10.1007/s40820-025-01845-7

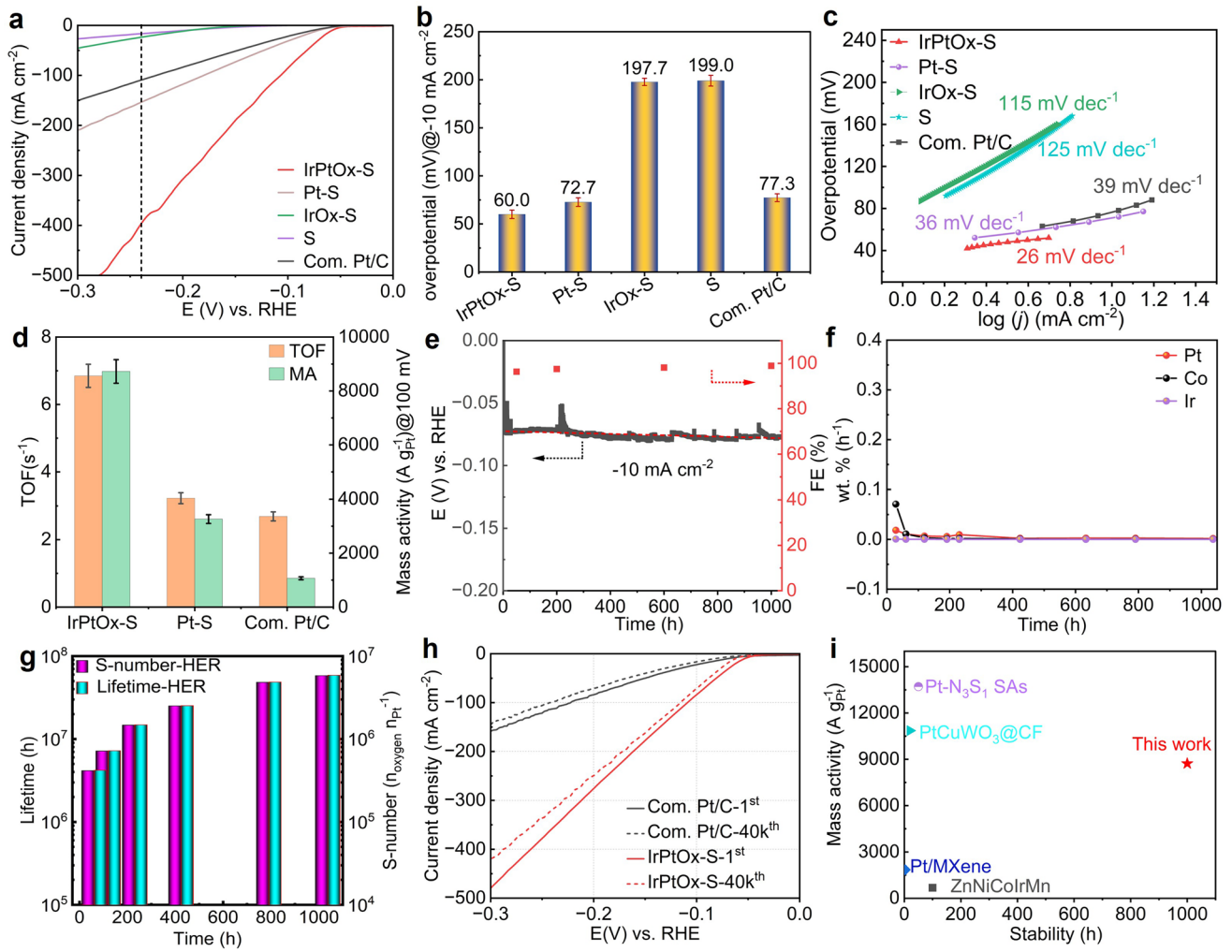

Fig. 5 Electrochemical HER of IrPtOx-S. **a** Polarization curves recorded on different samples using a three-electrode configuration in H_2-saturated 0.1 M $HClO_4$ electrolyte. Pt/Ir loading for IrPtOx-S, IrOx-S, and Pt–S was 10 $\mu g_{Pt/Ir}$ cm^{-2}, respectively. The loading of support material (S) was 150 ug cm^{-2}. Pt loading for Com. Pt/C was 20 ug_{Pt} cm^{-2}. **b** overpotential at − 10 mA cm^{-2} current density for different samples. **c** The relevant Tafel plots of the catalysts studied in (**a**). **d** Pt mass activities and TOF of different catalysts at an overpotential of 100 mV. **e** Chronoamperometric measurement on IrPtOx-S at − 10 mA cm^{-2} current density for 1040 h in H_2-saturated 0.5 M H_2SO_4 electrolyte, and the FE as function of time. **f** The corresponding ICP-MS measurements and **g** S-number and lifetime calculation during Chronoamperometric measurement shown in (**e**). **h** Polarization curves of $IrPtO_x$-S before and after 40,000 CV cycles from 0.0 to − 0.8 V vs. RHE in H_2-saturated 0.5 M H_2SO_4 electrolyte. **i** Comparison of S-number and Pt mass activity of $IrPtO_x$-S to those of reported Pt-based and Ir-based HER catalysts

(2.69 ± 0.13 s^{-1}, 1069.0 ± 60 A g_{Pt}^{-1}) (Fig. 5d), respectively. These results highlight the exceptional intrinsic activity of the IrPtOx-S catalyst for HER.

Long-term stability was confirmed via CA testing at − 10 mA cm^{-2} for 1040 h, with only a 4 mV increase in potential at the end of test (Fig. 5e). GC and ICP-MS measurements confirmed high H_2 purity (> 99.0% FE) and almost negligible metal dissolution rates throughout the test (Fig. 5e, f). Furthermore, we measured the FE at various current densities for both HER and OER (Fig. S11). The results demonstrate that $IrPtO_x$-S maintains high selectivity (> 98.6% FE) for both reactions even at elevated current densities. The S-number and lifetime for HER reached 5.8×10^6 n_{O2} n_{Ir}^{-1} and 6.0×10^7 h, respectively (Fig. 5g), ranking the $IrPtO_x$-S catalyst among the best HER catalysts reported [68]. AST involving 40,000 CV cycles scanning from 0 to − 0.8 V further demonstrated the high durability of $IrPtO_x$-S, with only an 8 mV increase in overpotential at 10 mA cm^{-2} after testing (Fig. 5h), superior to that of Pt/C. The comparison of S-number and MA for HER of the IrPtOx-S catalyst to

the reported Pt-based HER catalysts is shown in Fig. 5i and Table S3, underscoring its exceptional performance.

A comprehensive study of the ECSA of $IrPtO_x$-S conducted via double-layer capacitance (C_{dl}) measurements, H-UPD, and redox-active surface charge analysis reveals that IrPtOx-S exhibits a relatively higher ECSA compared to Com. IrO_2 and Pt/C (Figs. S12 and S13, Table S4). IrPtOx-S exhibited high specific activity for overall water splitting, confirming its robust intrinsic catalytic activity for both HER and OER (Figs. S14 and S15). Notably, compared to its OER-specific activity, $IrPtO_x$-S displayed a more pronounced enhancement in HER-specific activity across all tested catalysts, including the benchmark. This highlights that the role of Ir in optimizing Pt's catalytic activity for HER is more effective than Pt's contribution to enhancing Ir's activity for OER. We speculate that the incorporation of Pt into Ir significantly increased the ECSA of Ir species, potentially due to structural or electronic synergies between the two elements. The material's hierarchical porosity, high surface area, large ECSA, fast kinetics, high concentration of oxygen vacancies, and intimate electronic interactions between Ir and Pt, combined with the intrinsic self-catalytic activity of the support (Fig. S16), collectively contribute to its exceptional bifunctional activity for OER and HER in acidic media.

3.3 Performance of IrPtOx-S Under Realistic PEMWE Conditions

High catalytic activity observed in three-electrode systems (e.g., rotating disk electrode) does not necessarily correlate with performance in PEMWE, as the operating environments differ significantly in terms of electrode structure, temperature, pressure, and electrolyte. Therefore, evaluating catalysts under realistic PEMWE conditions is essential for practical applications. When operating under realistic PEMWE conditions, the hierarchical pore structure and electronic conductivity of the catalyst become critical for exposing active sites to reactants and electrolytes, managing water and product flow, and enabling fast electron transfer.

We fabricated the $IrPtO_x$-S catalyst into a membrane electrode assembly (MEA) serving as both the anode (OER) and cathode (HER) (referred to as MEA3) and investigated its bifunctional performance in a PEMWE single cell at 80 °C and ambient pressure (Fig. 6a). To separately evaluate OER and HER activities, we prepared two additional MEAs: $IrPtO_x$-S catalyst as the anode and Pt/C as the cathode (referred to as MEA1); and IrO_2/NbO_2 as the anode and $IrPtO_x$-S catalyst as the cathode (referred to as MEA2). A benchmark MEA0 was prepared using IrO_2/NbO_2 as the anode and Pt/C as the cathode. For the commercial catalysts, e.g., IrO_2/NbO_2 and Pt/C, the Ir and Pt loadings for the corresponding MEAs were set at 0.2 and 0.3 mg cm^{-2}, respectively. For our catalyst, the Ir and Pt loadings were significantly reduced to 0.075 mg cm^{-2}, highlighting its efficiency and cost-effectiveness.

As shown in Fig. 6b, MEA1 demonstrated superior performance compared to MEA0, achieving 1 A cm^{-2} at 1.63 V and 2 A cm^{-2} at 1.78 V. In contrast, MEA0 achieved 1 A cm^{-2} at 1.74 V and 2 A cm^{-2} at 1.91 V. This confirms the higher OER activity of $IrPtO_x$-S compared to IrO_2/NbO_2 under realistic PEMWE conditions. MEA2 showed slightly higher water splitting activity than MEA0, indirectly demonstrating the superior HER activity of the IrPtOx-S to that of Pt/C. Notably, the Pt loading in the cathode of MEA2 was only ¼ that of Pt in MEA0, further underscoring the efficiency of the $IrPtO_x$-S. The performance difference between MEA1 and MEA0 was more pronounced than that between MEA2 and MEA0, as the overall PEMWE performance is predominantly determined by the OER activity at the anode.

MEA3, with $IrPtO_x$-S at both electrodes, exhibited the best overall performance, achieving 1 A cm^{-2} at 1.60 V and 2 A cm^{-2} at 1.72 V. The Ir mass activity of MEA3 reached 116.3 A mg_{Ir}^{-1} at 1.7 V, approximately 5.6 times higher than that of MEA0 (Fig. 6c). Additionally, MEA3 achieved an electrical efficiency of 72.2% at 2.0 A cm^{-2}, with energy consumption of 43.1 kWh $kg^{-1}H_2$ at 1 A cm^{-2} and 46.0 kWh $kg^{-1}H_2$ at 2 A cm^{-2}. In contrast, MEA0 consumed 46.6 kWh $kg^{-1}H_2$ at 1 A cm^{-2} and 51.2 kWh $kg^{-1}H_2$ at 2 A cm^{-2}, corresponding to an efficiency of 64.7% at 2 A cm^{-2}. In addition, at the same applied potential, e.g., 1.72 V, our MEA reduces the cost per kilowatt by over 70% compared to the leading commercial catalyst. For instance, our MEA3 achieves a cost of \$7.85 kW^{-1}, whereas MEA0 incurs a significantly higher cost of \$25.19 kW^{-1}. The high BET surface area of $IrPtO_x$-S ensures sufficient exposure of active sites, directly enhancing catalytic activity. Furthermore, its hierarchical porosity, comprising interconnected micropores

 https://doi.org/10.1007/s40820-025-01845-7

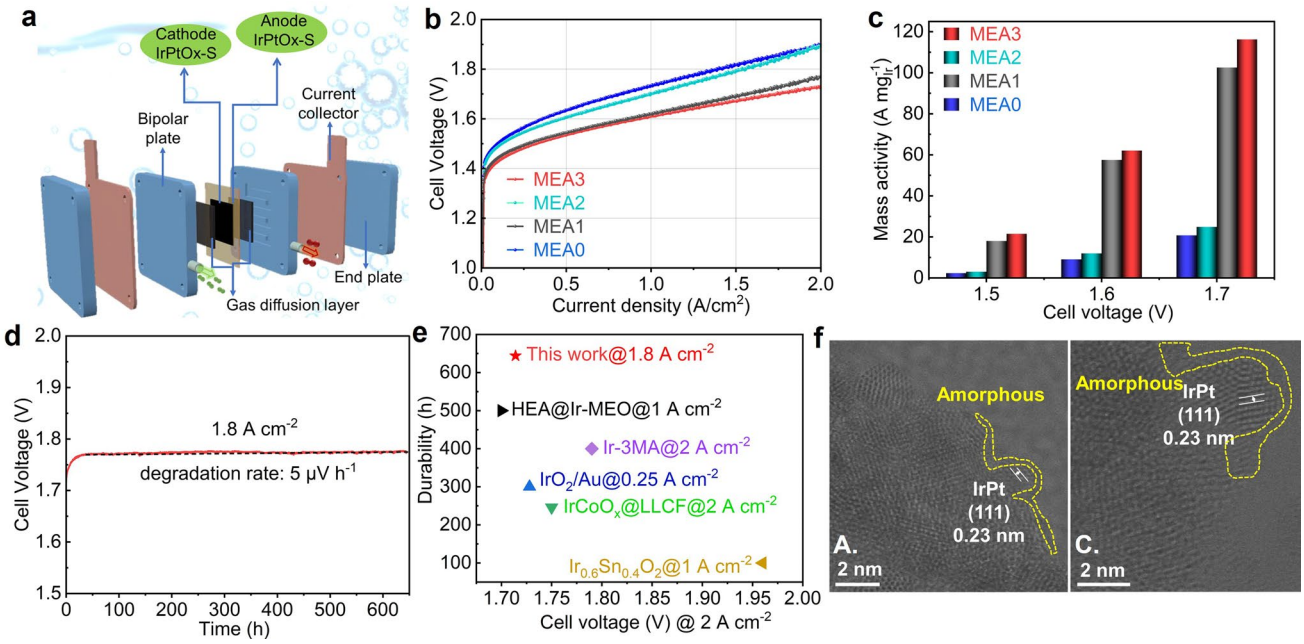

Fig. 6 PEMWE performance: **a** Schematic of the PEMWE device we used for this study. **b** Polarization curves of different MEAs. **c** Comparison of Ir mass activity of MEA0-MEA3 at different selected voltages. **d** Long-term durability test of MEA3 at 1.8 A cm^{-2} current density with 0.075 mg_{Ir} cm^{-2} at anode and 0.075 mg_{Pt} cm^{-2} at cathode. **e** Comparison of Ir mass activity and cell durability of MEA3 to the reported ones. **f** TEM images of IrPtOx-S peeled off from MEA3 after long-term durability test. A. denotes anode, and C. denotes cathode

and mesopores, facilitates influx of water molecules to active sites and promotes efflux of generated H_2/O_2 gas, thereby minimizing diffusion limitations and accelerating reaction kinetics, consequently a rapid mass transport. The synergy between high surface area (maximizing active-site accessibility) and hierarchical porosity (optimizing mass transport) enables sustained high current density (e.g., 2 A cm^{-2} at 1.72 V, Fig. 6b), even at elevated potentials. Additionally, the oxygen vacancy-rich structure (Fig. 2d) enhances electronic conductivity, which improves charge transfer efficiency and further boosts catalytic activity. Collectively, those advantages are reflected in the lower and more stable cell impedance of PEMWE with MEA3 as compared to PEMWE with MEA0 (Fig. S17).

MEA3 was subjected to a 646-h durability test at 1.8 A cm^{-2}, demonstrating exceptional stability with an average degradation rate of 5 μV h^{-1} (Fig. 6d). Based on the U.S. Department of Energy (DOE) protocol, which defines lifetime as the time until a 10% voltage loss from the beginning-of-life operation [10], MEA3 can operate at 1.8 A m^{-2} for at least 34,360 h with ultralow loadings of 0.075 mg_{Ir} cm^{-2} at the anode and 0.075 mg_{Pt} cm^{-2} at the cathode. This exceptional performance positions the $IrPtO_x$-S as a leading candidate for industrial PEMWE applications.

The performance metrics of IrPtOx-S, including lifetime and cell voltage at 2 A cm^{-2} current density under PEMWE conditions, were compared to those of reported catalysts (Fig. 6e, Table S3). MEA3 outperformed most Ir- and Pt-based MEAs, establishing itself as one of the best bifunctional catalysts for PEMWE (Fig. 6e). STEM-EDS characterization of IrPtOx-S peeled off from the anode and cathode of MEA3 after a 646-h durability test revealed no evidence of particle agglomeration or separation (Figs. S18 and S19). STEM-EDS line-scan profile (Fig. S18b, c) and HRTEM analysis (Fig. 6f) revealed no significant particle size change, aside from a minor increase in the thickness of $IrPtO_x$ species, demonstrating exceptional structural stability under extended PEMWE operating conditions. XPS results revealed partial oxidation of surface Ir, as indicated by the increased proportion of Ir (IV) at the anode after the durability test (Fig. 2a), while negligible changes for Pt, Co, and O (Figs. 2b, c and S20). Raman spectroscopy further confirmed the structural integrity of the post-stability $IrPtO_x$-S, with broader and weaker peaks (Fig. S21) indicating amorphization or reduced particle size, consistent with TEM observations (Fig. 6f).

3.4 Mechanistic Insights into the Origin of Catalytic Activity

To investigate the active sites and monitor the evolution of chemical oxidation states during OER and HER, we performed in situ XANES and EXAFS experiments at the Ir L_{III}, Pt L_{III}, and Co K edges on IrPtOx-S. The sequence of applied potentials during OER and HER is illustrated in Fig. 7.

Under OER conditions, the WL position at the Ir L_{III} edge at open circuit potential (OCP) showed a slight positive shift compared to the IrPtOx powder, likely due to the adsorption of H_2O molecules in the electrolyte, causing electron delocalization (Figs. 3a and 7a). As the potential increased to 1.38 V, the WL position shifted to higher energy by 0.5 eV, accompanied by an increase in WL intensity (Fig. 7a, inset), indicating the oxidation of Ir sites. At 1.7 V, the WL peak position remained unchanged, but the intensity increased slightly, suggesting a slightly increased 5*d* hole states [69], a feature of higher activity. Compared to the dry sample (Fig. 3a), the Ir L_{III} WL peak positions at 1.38 and 1.70 V were close to that of IrO_2 reference, implying an increased fraction of Ir(IV) during the OER process. Previous studies have demonstrated that the formation of Ir(III) intermediates contributes to the instability of Ir-based catalysts [70]. The stability of $IrPtO_x$-S is enhanced by the rapid conversion of Ir^0 to Ir(IV). Given that XANES is a bulk-sensitive analytical technique, the white line energies represent average values of the oxidized iridium atoms in the shell and the metallic iridium atoms in the IrPt core. Therefore, the slight upshift of the WL energy upon the formation of the iridium oxide shell indicates that the contribution of the metallic bulk remains pronounced. When the potential reversed to OCP, the high oxidation state of Ir was retained (Fig. 7a, inset). Iridium in high oxidation states (e.g., Ir^{4+}, Ir^{5+}) exhibits strong electrophilic character, optimizing the binding strength of oxygen-containing intermediates (*OH, *O, *OOH) critical for oxygen evolution. Additionally, Fourier transform (FT) analysis of the Ir L_{III}-edge EXAFS spectrum for the dry sample reveals an average Ir–Ir/Pt bond

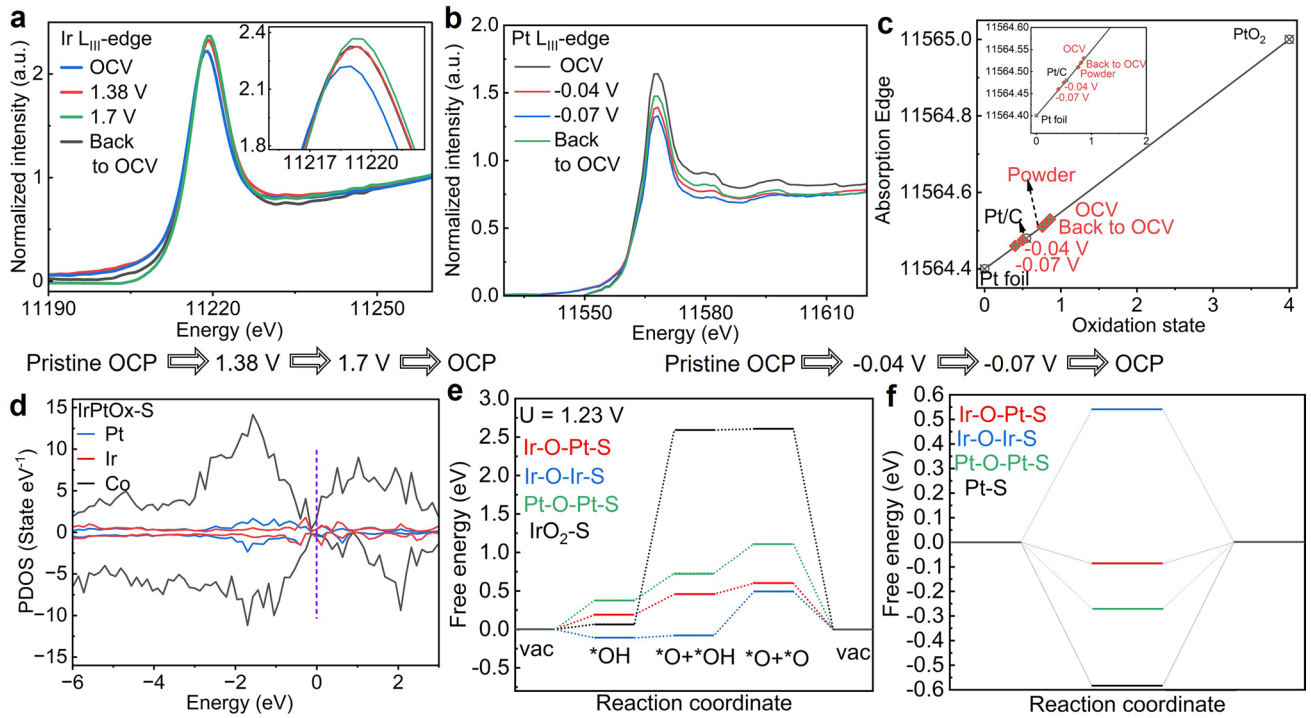

Fig. 7 In situ XANES analysis and theoretical study of IrPtOx-S for OER and HER. **a** Ir L_{III} edge XANES measured in 0.1 M $HClO_4$ during OER at OCV, 1.38V, 1.70 V, and reverse to OCV. Inset is the enlargement of the white line portion. **b** Pt L_{III} edge XANES measured in 0.5 M H_2SO_4 during HER at OCV, −0.04V, −0.07 V, and reverse to OCV. **c** Calculated Pt valence state based on the first differential of the absorption peak shown in **b.** Pt foil, Pt/C, and PtO_2 were the references. **d** PDOS of Ir 5d, Pt 5d, and Co 3d of IrPtOx-S. **e** Gibbs free energy ($\Delta G_{absorbates}$*) diagrams of OER through bi-nuclear reaction mechanism for IrPtOx-S including Ir–O–Pt, Ir–O–Ir, and Pt–O–Pt sites and for IrO_2-S. U = 1.23 V vs. RHE. **f** ΔG_H* of HER at the equilibrium potential for IrPtOx-S including Ir–O–Pt, Ir–O–Ir, and Pt–O–Pt sites and for Pt–S

https://doi.org/10.1007/s40820-025-01845-7

length of 2.75 Å (Figs. 3b and S22, Table S5), consistent with a configuration that facilitates direct O–O coupling (2.4–2.9 Å)—a bi-nuclear pathway [44]. By contrast, fitting IrO_2 shows an Ir–Ir bond length of 3.22 Å. Therefore, promoting the oxidation of Ir to higher valence states may enhance both OER activity and durability of $IrPtO_x$-S by enabling a bi-nuclear reaction pathway.

Under HER conditions, the Pt L_{III} edge WL intensity at OCP appeared enhanced compared to the IrPtOx-S powder (Figs. 3d and 7b), similar to the observation at the Ir L_{III} edge. This phenomenon is attributed to the adsorption of hydrogen (H_{ads}), which increases the d-band hole count, reflected in the increased WL intensity [71]. As the applied potential became more negative, the WL intensity decreased (Fig. 7b), indicating the reduction of Pt to lower oxidation states. A similar trend was observed for PtW_6O_{24}/C during HER [72]. By plotting the differential of the absorption peak against the oxidation states of reference materials, the average oxidation state of Pt during HER was estimated to be around + 0.5 (− 0.04 V) and + 0.4 (− 0.07 V) (Fig. 7c), lower than that of Pt in the IrPtOx-S powder (Fig. 7c, inset), likely due to the reduction process during HER. The oxidation state of Pt reversed to a value comparable to that of Pt in the $IrPtO_x$-S powder when the potential returned to OCP. Note that XANES represents the average values of the oxidation state of a given material, and based on our XPS analysis, the oxidation state of the oxidized Pt in the $IrPtO_x$-S is approximately Pt(II), with metallic Pt dominating the $IrPtO_x$-S. Pt(II) exhibits superior electrocatalytic activity for HER compared to Pt(0), as the Pt-O bond facilitates proton-electron coupling and accelerates H_2 release [72]. In summary, partial Ir and Pt in the Ir–Pt alloy and the amorphous regions evolved into relatively higher valence states and a stable structure, forming Ir-O-Pt bonds wrapped outside the IrPt nanoparticles during water splitting. These bonds serve as active sites for OER and HER, respectively.

In acidic media, HER proceeds via the Volmer–Heyrovsky or Volmer–Tafel mechanisms, distinguished by the Tafel slope. The Tafel slope of the $IrPtO_x$-S for HER is 26 mV dec^{-1} (Fig. 5c), indicating that the Tafel step in the Volmer–Tafel mechanism is the rate-determining step [45]. For OER, three reaction pathways are possible: AEM, LOM, and oxide pair mechanism (OPM) [43]. To experimentally investigate the LOM pathway, we used in situ mass spectrometry (MS) with isotope labeling. IrPtOx-S was pretreated in 0.1 M $HClO_4$ with $H_2{}^{18}O$ as the solvent to label the sample with ^{18}O. The sample was then used to catalyze water oxidation at 15 mA cm^{-2} for 30 min in 0.1 M $HClO_4$ with $H_2{}^{16}O$ as the solvent (Fig. S23a). The ratios of $^{36}O_2/^{32}O_2$ in the produced oxygen were measured to be ~ 0.2% (Fig. S23b), similar to the natural abundance of ^{18}O [73]. In situ XANES spectra at the O K-edge showed negligible changes at OCP and under various applied potentials (Fig. S24), suggesting that lattice oxygen does not participate in the OER reaction. These results exclude the LOM mechanism.

To further understand the OER and HER mechanisms, we performed DFT calculations. The projected density of states (pDOS) of the Ir, Pt, and Co d-bands in $IrPtO_x$-S revealed new hybridized electronic states and charge redistribution compared to IrOx-S and Pt–S (Figs. 7d and S25), indicating strong electronic interactions between Ir–Pt and the host. Specifically, the electron density of Pt in IrPtOx-S decreased, and the d-band center shifted negatively from − 0.094 eV (Pt–S) to − 2.438 eV ($IrPtO_x$-S), weakening hydrogen chemisorption on Pt and enhancing HER kinetics [74]. Additionally, the pDOS showed increased electron density of Ir and Co near the Fermi level (≈ 0 to − 1 eV), suggesting more dangling bonds or active electronic states (Fig. S25). The d-band centers of Ir and Co in IrPtOx-S were upshifted (Ir: − 2.950 eV, Co: − 2.065 eV) relative to those in IrOx-S (Ir: − 3.866 eV, Co: − 2.398 eV), enhancing the interaction between active sites and adsorbates and reducing kinetic barriers for intermediate formation [69]. The overlapping Ir 5*d*, Pt 5*d*, and Co 3*d* orbitals further confirmed strong electronic interactions among these elements. Furthermore, Bader charge analysis reveals significant electronic interaction between Ir and Pt (Table S6), characterized by charge redistribution. This interaction balances the binding strength of key OER intermediates—mitigating over-binding at Ir–O–Ir sites and strengthening under-binding at Pt–O–Pt sites—thereby optimizing adsorption energetics and enhancing overall OER and HER activities.

The energetics of all intermediates (*OH, *O, *OOH, where * denotes an active site) during OER for each elementary step were calculated at an applied potential of 1.23 V vs. RHE (Fig. 7e). For the traditional AEM mechanism, there is a constant energy difference of 3.2 eV between *OH and *OOH that limits the exploration of more active electrocatalysts for water electrolysis. In this work, we adopt the bi-nuclear mechanism for OER, where the formation of problematic *OOH specie would be avoided, and a lower overpotential could be achieved [42]. Based on our

experimental results, we employed Ir–O–Pt, Ir–O–Ir, and Pt–O–Pt configurations as the active sites for simulations, respectively, with IrO_2-S (OER) and Pt–S (HER) serving as benchmarks (Figs. S26 and S27). For OER on IrPtOx-S, the rate-determining step (RDS) is the first deprotonation of *OH to *O, exhibiting an exceptionally low activation energy barrier of 0.26 eV (Fig. 7e). In contrast, the RDS for OER on Ir-O-Ir shifts to the second deprotonation of *OH to *O, with the energy barrier increasing to 0.58 eV. Similarly, the RDS for OER on Pt–O–Pt is the same as that of Ir–O–Ir, but its energy barrier rises further to 0.67 eV. These results strongly suggest that Ir–O–Pt is the dominant active site, responsible for the superior OER activity of $IrPtO_x$-S. Notably, the benchmark catalyst IrO_2-S shares the same RDS as Ir–O–Pt but displays the highest activation barrier (2.53 eV) among all studied catalysts. This stark contrast underscores the unique efficiency of the Ir–O–Pt configuration. Additionally, IrO_2-S might follow an AEM mechanism [29].

For HER, the adsorption free energy of H* (ΔGH^*) is a key descriptor of activity in acidic media, with values closer to zero indicating higher activity [75]. $IrPtO_x$-S showed significantly improved HER activity compared to Pt–S (Fig. 7f), highlighting the intimate interaction between Pt and Ir, as well as the importance of the Ir–O–Pt structure. As shown in Fig. 7f, ΔG_H^* for the Ir–O–Pt site (− 0.14 eV) was closer to the ideal ($\Delta GH^* = 0$ eV) compared to Ir–O–Ir (0.54 eV) and Pt–O–Pt (− 0.27 eV). This confirms that the Ir-O-Pt site is directly responsible for both optimizing hydrogen binding energetics and driving the exceptional HER activity of $IrPtO_x$-S, as its near-ideal ΔG_H^* minimizes kinetic barriers during hydrogen evolution. Notably, the LaNi-Co_3O_4 (S) substrate itself exhibits inherent catalytic activity for both OER and HER, as confirmed by experimental characterizations and DFT simulations (Figs. S16 and S28). The in situ XANES characterizations combined with DFT simulations reveal that the exceptional bifunctional OER and HER performance of $IrPtO_x$-S in acidic media arises from the catalytic synergy between $IrPtO_x$ and substrate (S), and the optimized charge redistribution between Ir and Pt, which are bridged by O ligands, promoting the bi-nuclear and the Volmer–Tafel mechanism for OER and HER with reduced energy barriers. Additionally, the metal–support interaction along with the intimate affinity between Ir and Pt enables the formation of the unique $IrPtO_x$ shell–IrPt core structure, expediting electron transfer for OER and HER to proceed.

4 Conclusions

In this study, we developed a highly efficient and durable bifunctional catalyst, $IrPtO_x$-S, for both OER and HER in acidic media. The catalyst demonstrated exceptional performance in PEMWE device, achieving a current density of 2 A cm^{-2} at 1.72 V with ultralow precious metal loadings (0.075 mg_{Ir} cm^{-2} Ir at the anode and 0.075 mg_{Pt} cm^{-2} Pt at the cathode). The IrPtOx-S exhibited remarkable stability, sustaining OER and HER for over 646 h in a PEMWE single cell with low average degradation rate of 5 μV h^{-1}, outperforming most reported Ir- and Pt-based catalysts (Table S3).

Advanced characterization techniques, including in situ XANES, EXAFS, and DFT simulations, revealed that the high activity and stability of IrPtOx-S stem from the optimized charge redistribution between Ir and Pt, as well as the unique IrPt core–IrPtOx shell structure. The Ir sites and Pt sites bridged by O ligands, namely Ir–O–Pt sites, served as active sites promoting the bi-nuclear mechanism for OER and Volmer–Tafel mechanism for HER. The optimized charge redistribution and electronic structure reduced kinetic barriers for both OER and HER, while the unique metal core–oxide shell structure, abundant oxygen vacancies, hierarchical porosity, and high electrochemical surface area further enhanced electron and mass transfer, contributing to the catalyst's superior performance.

This work not only provides a cost-effective solution for green hydrogen production but also offers fundamental insights into the design of high-performance bifunctional catalysts for PEMWE. The exceptional activity, durability, and industrial applicability of IrPtOx-S position it as a leading candidate for advancing PEMWE technology toward commercialization and achieving global decarbonization goals. By addressing the critical challenges of precious metal usage and catalyst stability, this study paves the way for the widespread adoption of PEMWE in renewable energy systems, marking a significant step toward achieving global decarbonization goals.

Acknowledgements This work is supported by overseas Outstanding Youth Science Fund Project provided by National Natural Science Foundation of China (NSFC) under contract No. 22Z990204807, Natural Sciences—Basic Research Special Zone Program provided by shanghai government under contract No. 22Z511203738, Key Open Fund Project provided by Shaoxing New Energy and Molecular Engineering Research Institute, Shanghai Jiao Tong University under contract No. 22H010103236, and Sinopec Natural Science research project provided by Sinopec

 https://doi.org/10.1007/s40820-025-01845-7

research institute of petroleum processing under contract No. 23H010100026. Z.W thanks the support from National Science Foundation of China (22309113) and Scientific and Technological Project of Yunnan Precious Metals Laboratory (YPML-20240502029). The authors acknowledge the support provided by Beamlines BL14W1 and BL08U1 at the Shanghai Synchrotron Radiation Facility (SSRF) and the ODE beamline at the Source Optimisée de Lumière à Energie Intermédiaire du LURE (SOLEIL), France. We acknowledge Dr. Zheng Wang for his help with the DFT simulation. We would also like to express our gratitude to the Instrumental Analysis Center at Shanghai Jiao Tong University (SJTU).

Author Contributions L.C. designed research and managed the projects; Y.L. performed experiments; Z. W., X.E., and F. Y. performed DFT; X.W., P.L., X. Z., Y.Q., and Y.Y conducted TEM; L.C. and Y.L. analyzed data; W.W. and T. Z helped with the experiments; and L.C., Y.L., F.H., and W.D. wrote the paper.

Declarations

Conflict of Interests The authors declare no interest conflict. They have no known competing financial interests or personal relationships that could have appeared to influence the work reported in this paper.

Supplementary Information The online version contains supplementary material available at https://doi.org/10.1007/s40820-025-01845-7.

References

1. C.R. Wang, J.M. Stansberry, R. Mukundan, H.J. Chang, D. Kulkarni et al., Proton exchange membrane (PEM) water electrolysis: cell-level considerations for gigawatt-scale deployment. Chem. Rev. **125**(3), 1257–1302 (2025). https://doi.org/10.1021/acs.chemrev.3c00904
2. A. Odenweller, F. Ueckerdt, The green hydrogen ambition and implementation gap. Nat. Energy **10**(1), 110–123 (2025). https://doi.org/10.1038/s41560-024-01684-7
3. S.J. Davis, N.S. Lewis, M. Shaner, S. Aggarwal, D. Arent et al., Net-zero emissions energy systems. Science **360**(6396), eaas9793 (2018). https://doi.org/10.1126/science.aas9793
4. P. Wolfram, P. Kyle, J. Fuhrman, P. O'Rourke, H. McJeon, The hydrogen economy can reduce costs of climate change mitigation by up to 22%. One Earth **7**(5), 885–895 (2024). https://doi.org/10.1016/j.oneear.2024.04.012
5. Hydrogen Council, McKinsey & Company, Hydrogen Insights 2023 (2023). https://hydrogencouncil.com/en/hydrogen-insights-2023-december-update/
6. DECHEMA, acatech, Comparative Analysis of International Hydrogen Strategies (2024). https://www.wasserstoff-kompass.de/fileadmin/user_upload/img/news-und-media/dokumente/2023_e_H2_Laenderanalyse.pdf
7. C. Minke, M. Suermann, B. Bensmann, R. Hanke-Rauschenbach, Is iridium demand a potential bottleneck in the realization of large-scale PEM water electrolysis? Int. J. Hydrog. Energy **46**(46), 23581–23590 (2021). https://doi.org/10.1016/j.ijhydene.2021.04.174
8. F. Zeng, C. Mebrahtu, L. Liao, A.K. Beine, R. Palkovits, Stability and deactivation of OER electrocatalysts: a review. J. Energy Chem. **69**, 301–329 (2022). https://doi.org/10.1016/j.jechem.2022.01.025
9. Y. Wang, Y. Pang, H. Xu, A. Martinez, K.S. Chen, PEM Fuel cell and electrolysis cell technologies and hydrogen infrastructure development–a review. Energy Environ. Sci. **15**(6), 2288–2328 (2022). https://doi.org/10.1039/D2EE00790H
10. U.S. Department of Energy. Technical targets for proton exchange membrane electrolysis (2024). https://www.energy.gov/eere/fuelcells/technical-targets-proton-exchange-membrane-electrolysis
11. I. Roger, M.A. Shipman, M.D. Symes, Earth-abundant catalysts for electrochemical and photoelectrochemical water splitting. Nat. Rev. Chem. **1**, 0003 (2017). https://doi.org/10.1038/s41570-016-0003
12. X. Shang, J.-H. Tang, B. Dong, Y. Sun, Recent advances of nonprecious and bifunctional electrocatalysts for overall water splitting. Sustain. Energy Fuels **4**(7), 3211–3228 (2020). https://doi.org/10.1039/D0SE00466A
13. M. Ali Raza Anjum, M.S. Okyay, M. Kim, M.H. Lee, N. Park et al., Bifunctional sulfur-doped cobalt phosphide electrocatalyst outperforms all-noble-metal electrocatalysts in alkaline electrolyzer for overall water splitting. Nano Energy **53**, 286–295 (2018). https://doi.org/10.1016/j.nanoen.2018.08.064
14. H. Wang, H.-W. Lee, Y. Deng, Z. Lu, P.-C. Hsu et al., Bifunctional non-noble metal oxide nanoparticle electrocatalysts through lithium-induced conversion for overall water splitting. Nat. Commun. **6**, 7261 (2015). https://doi.org/10.1038/ncomms8261
15. J. Luo, J.H. Im, M.T. Mayer, M. Schreier, M.K. Nazeeruddin et al., Water photolysis at 12.3% efficiency via perovskite photovoltaics and earth-abundant catalysts. Science **345**(6204), 1593–1596 (2014). https://doi.org/10.1126/science.1258307

16. F.-Y. Chen, Z.-Y. Wu, Z. Adler, H. Wang, Stability challenges of electrocatalytic oxygen evolution reaction: from mechanistic understanding to reactor design. Joule **5**(7), 1704–1731 (2021). https://doi.org/10.1016/j.joule.2021.05.005
17. L. She, G. Zhao, T. Ma, J. Chen, W. Sun et al., On the durability of iridium-based electrocatalysts toward the oxygen evolution reaction under acid environment. Adv. Funct. Mater. **32**(5), 2108465 (2022). https://doi.org/10.1002/adfm.202108465
18. J.K. Nørskov, J. Rossmeisl, A. Logadottir, L. Lindqvist, J.R. Kitchin et al., Origin of the overpotential for oxygen reduction at a fuel-cell cathode. J. Phys. Chem. B **108**(46), 17886–17892 (2004). https://doi.org/10.1021/jp047349j
19. C. Liu, I. Roh, H.S. Park, B.J. Park, T. Yu, IrPt alloy nanoparticles with controllable compositions as catalysts for electrochemical oxygen and hydrogen evolution. ACS Appl. Nano Mater. **5**(11), 17152–17158 (2022). https://doi.org/10.1021/acsanm.2c04069
20. F. Andolfatto, R. Durand, A. Michas, P. Millet, P. Stevens, Solid polymer electrolyte water electrolysis: electrocatalysis and long-term stability. Int. J. Hydrog. Energy **19**(5), 421–427 (1994). https://doi.org/10.1016/0360-3199(94)90018-3
21. D.B. Rogers, R.D. Shannon, A.W. Sleight, J.L. Gillson, Crystal chemistry of metal dioxides with rutile-related structures. Inorg. Chem. **8**(4), 841–849 (1969). https://doi.org/10.1021/ic50074a029
22. T. Ioroi, N. Kitazawa, K. Yasuda et al., IrO_2-deposited Pt electrocatalysts for unitized regenerative polymer electrolyte fuel cells. J. Appl. Electrochem. **31**, 1179–1183 (2001). https://doi.org/10.1023/A:1012755809488
23. F.-D. Kong, S. Zhang, G.-P. Yin, N. Zhang, Z.-B. Wang et al., Pt/porous-IrO_2 nanocomposite as promising electrocatalyst for unitized regenerative fuel cell. Electrochem. Commun. **14**(1), 63–66 (2012). https://doi.org/10.1016/j.elecom.2011.11.002
24. W. Yao, J. Yang, J. Wang, Y. Nuli, Chemical deposition of platinum nanoparticles on iridium oxide for oxygen electrode of unitized regenerative fuel cell. Electrochem. Commun. **9**(5), 1029–1034 (2007). https://doi.org/10.1016/j.elecom.2006.12.017
25. R.E. Fuentes, H.R. Colón-Mercado, M.J. Martínez-Rodríguez, Pt-Ir/TiC electrocatalysts for PEM fuel cell/electrolyzer process. J. Electrochem. Soc. **161**(1), F77–F82 (2014). https://doi.org/10.1149/2.050401jes
26. S.-D. Yim, G.-G. Park, Y.-J. Sohn, W.-Y. Lee, Y.-G. Yoon et al., Optimization of PtIr electrocatalyst for PEM URFC. Int. J. Hydrog. Energy **30**(12), 1345–1350 (2005). https://doi.org/10.1016/j.ijhydene.2005.04.013
27. M.K. Debe, S.M. Hendricks, G.D. Vernstrom, M. Meyers, M. Brostrom et al., Initial performance and durability of ultra-low loaded NSTF electrodes for PEM electrolyzers. J. Electrochem. Soc. **159**(6), K165–K176 (2012). https://doi.org/10.1149/2.065206jes
28. H.S. Oh, H.N. Nong, T. Reier, A. Bergmann, M. Gliech et al., Electrochemical catalyst-support effects and their stabilizing role for IrO_x nanoparticle catalysts during the oxygen evolution reaction. J. Am. Chem. Soc. **138**(38), 12552–12563 (2016). https://doi.org/10.1021/jacs.6b07199
29. L. Chong, J. Wen, E. Song, Z. Yang, I.D. Bloom et al., Synergistic Co─Ir/Ru composite electrocatalysts impart efficient and durable oxygen evolution catalysis in acid. Adv. Energy Mater. **13**(37), 2302306 (2023). https://doi.org/10.1002/aenm.202302306
30. P. Thangavel, M. Ha, S. Kumaraguru, A. Meena, A.N. Singh et al., Graphene-nanoplatelets-supported NiFe-MOF: high-efficiency and ultra-stable oxygen electrodes for sustained alkaline anion exchange membrane water electrolysis. Energy Environ. Sci. **13**(10), 3447–3458 (2020). https://doi.org/10.1039/D0EE00877J
31. Y. Liang, Y. Li, H. Wang, J. Zhou, J. Wang et al., Co_3O_4 nanocrystals on graphene as a synergistic catalyst for oxygen reduction reaction. Nat. Mater. **10**(10), 780–786 (2011). https://doi.org/10.1038/nmat3087
32. Y.P. Zhu, T.Y. Ma, M. Jaroniec, S.Z. Qiao, Self-templating synthesis of hollow Co_3O_4 microtube arrays for highly efficient water electrolysis. Angew. Chem. Int. Ed. **56**(5), 1324–1328 (2017). https://doi.org/10.1002/anie.201610413
33. A.V. Avani, E.I. Anila, Recent advances of MoO_3 based materials in energy catalysis: applications in hydrogen evolution and oxygen evolution reactions. Int. J. Hydrog. Energy **47**(47), 20475–20493 (2022). https://doi.org/10.1016/j.ijhydene.2022.04.252
34. A. Meena, P. Thangavel, A.S. Nissimagoudar, A. Narayan Singh, A. Jana et al., Bifunctional oxovanadate doped cobalt carbonate for high-efficient overall water splitting in alkaline-anion-exchange-membrane water-electrolyzer. Chem. Eng. J. **430**, 132623 (2022). https://doi.org/10.1016/j.cej.2021.132623
35. A. Meena, P. Thangavel, D.S. Jeong, A.N. Singh, A. Jana et al., Crystalline-amorphous interface of mesoporous Ni_2P @ FePOxHy for oxygen evolution at high current density in alkaline-anion-exchange-membrane water-electrolyzer. Appl. Catal. B Environ. **306**, 121127 (2022). https://doi.org/10.1016/j.apcatb.2022.121127
36. A. Meena, G. Shin, S. Cho, A.N. Singh, A.T. Aqueel Ahmed et al., Engineering a synergistic CoMn-LDH/Fe_2O_3@NF heterostructure for highly efficient oxygen evolution reaction. Ceram. Int. **49**(23), 37929–37935 (2023). https://doi.org/10.1016/j.ceramint.2023.09.122
37. A. Meena, A. Jana, G. Shin, A.N. Singh, J.-W. Jang et al., Ultra-durable high-performance CoMo-MCA/Fe-NWs/NF heterostructures for industrial-grade current density seawater splitting. J. Mater. Chem. A **12**(43), 30022–30031 (2024). https://doi.org/10.1039/D4TA05175K
38. I.C. Man, H.-Y. Su, F. Calle-Vallejo, H.A. Hansen, J.I. Martínez et al., Universality in oxygen evolution electrocatalysis on oxide surfaces. ChemCatChem **3**(7), 1159–1165 (2011). https://doi.org/10.1002/cctc.201000397
39. L. Chong, G. Gao, J. Wen, H. Li, H. Xu et al., La- and Mn-doped cobalt spinel oxygen evolution catalyst for proton exchange membrane electrolysis. Science **380**(6645), 609–616 (2023). https://doi.org/10.1126/science.ade1499
40. Y. Zhao, P.V. Kumar, X. Tan, X. Lu, X. Zhu et al., Modulating Pt-O-Pt atomic clusters with isolated cobalt atoms for enhanced hydrogen evolution catalysis. Nat. Commun. **13**(1), 2430 (2022). https://doi.org/10.1038/s41467-022-30155-4

 https://doi.org/10.1007/s40820-025-01845-7

41. R.G. González-Huerta, G. Ramos-Sánchez, P.B. Balbuena, Oxygen evolution in Co-doped RuO_2 and IrO_2: experimental and theoretical insights to diminish electrolysis overpotential. J. Power. Sources **268**, 69–76 (2014). https://doi.org/10.1016/j.jpowsour.2014.06.029
42. M. Busch, Water oxidation: from mechanisms to limitations. Curr. Opin. Electrochem. **9**, 278–284 (2018). https://doi.org/10.1016/j.coelec.2018.06.007
43. Y. Nosaka, Molecular mechanisms of oxygen evolution reactions for artificial photosynthesis. Oxygen **3**(4), 407–451 (2023). https://doi.org/10.3390/oxygen3040027
44. Z.-H. Yin, H. Liu, J.-S. Hu, J.-J. Wang, The breakthrough of oxide pathway mechanism in stability and scaling relationship for water oxidation. Natl. Sci. Rev. **11**(11), nwae362 (2024). https://doi.org/10.1093/nsr/nwae362
45. J. Zhu, L. Hu, P. Zhao, L.Y.S. Lee, K.Y. Wong, Recent advances in electrocatalytic hydrogen evolution using nanoparticles. Chem. Rev. **120**(2), 851–918 (2020). https://doi.org/10.1021/acs.chemrev.9b00248
46. S. Zhao, H. Yu, R. Maric, N. Danilovic, C.B. Capuano et al., Calculating the electrochemically active surface area of iridium oxide in operating proton exchange membrane electrolyzers. J. Electrochem. Soc. **162**(12), F1292–F1298 (2015). https://doi.org/10.1149/2.0211512jes
47. S. Geiger, O. Kasian, M. Ledendecker, E. Pizzutilo, A.M. Mingers et al., The stability number as a metric for electrocatalyst stability benchmarking. Nat. Catal. **1**(7), 508–515 (2018). https://doi.org/10.1038/s41929-018-0085-6
48. G. Kresse, D. Joubert, From ultrasoft pseudopotentials to the projector augmented-wave method. Phys. Rev. B **59**(3), 1758–1775 (1999). https://doi.org/10.1103/physrevb.59.1758
49. J. Carrasco, J. Klimeš, A. Michaelides, The role of van der Waals forces in water adsorption on metals. J. Chem. Phys. **138**(2), 024708 (2013). https://doi.org/10.1063/1.4773901
50. J.P. Perdew, K. Burke, M. Ernzerhof, Generalized gradient approximation made simple. Phys. Rev. Lett. **77**(18), 3865–3868 (1996). https://doi.org/10.1103/physrevlett.77.3865
51. S.L. Dudarev, G.A. Botton, S.Y. Savrasov, C.J. Humphreys, A.P. Sutton, Electron-energy-loss spectra and the structural stability of nickel oxide: An LSDA+U study. Phys. Rev. B **57**(3), 1505–1509 (1998). https://doi.org/10.1103/physrevb.57.1505
52. H. Xu, D. Cheng, D. Cao, X.C. Zeng, Revisiting the universal principle for the rational design of single-atom electrocatalysts. Nat. Catal. **7**(2), 207–218 (2024). https://doi.org/10.1038/s41929-023-01106-z
53. P. Strasser, S. Koh, T. Anniyev, J. Greeley, K. More et al., Lattice-strain control of the activity in dealloyed core-shell fuel cell catalysts. Nat. Chem. **2**(6), 454–460 (2010). https://doi.org/10.1038/nchem.623
54. D. Chandra, D. Takama, T. Masaki, T. Sato, N. Abe et al., Highly efficient electrocatalysis and mechanistic investigation of intermediate $IrO_x(OH)_y$ nanoparticle films for water oxidation. ACS Catal. **6**(6), 3946–3954 (2016). https://doi.org/10.1021/acscatal.6b00621
55. S.J. Pennycook, Scanning transmission electron microscopy: Z-contrast imaging. Microsc. Microanal. **18**, 652–664 (2012). https://doi.org/10.1002/0471266965.com083.pub2
56. Y. Liu, X. Liu, A.R. Jadhav, T. Yang, Y. Hwang et al., Unraveling the function of metal–amorphous support interactions in single-atom electrocatalytic hydrogen evolution. Angew. Chem. Int. Ed. **61**(9), e202114160 (2022). https://doi.org/10.1002/anie.202114160
57. S. Butcha, S. Assavapanumat, S. Ittisanronnachai, V. Lapeyre, C. Wattanakit et al., Nanoengineered chiral Pt-Ir alloys for high-performance enantioselective electrosynthesis. Nat. Commun. **12**(1), 1314 (2021). https://doi.org/10.1038/s41467-021-21603-8
58. H. Wang, D. Wang, C. Sun, X. Zhao, C. Xu et al., Oriented generation of $1O_2$ from peroxymonosulfate via Co_3O_4 facet engineering. Appl. Catal. B Environ. Energy **364**, 124854 (2025). https://doi.org/10.1016/j.apcatb.2024.124854
59. J.-W. Yeh, S.-Y. Chang, Y.-D. Hong, S.-K. Chen, S.-J. Lin, Anomalous decrease in X-ray diffraction intensities of Cu–Ni–Al–Co–Cr–Fe–Si alloy systems with multi-principal elements. Mater. Chem. Phys. **103**(1), 41–46 (2007). https://doi.org/10.1016/j.matchemphys.2007.01.003
60. J.J. Velasco-Vélez, E.A. Carbonio, C.H. Chuang, C.J. Hsu, J.F. Lee et al., Surface electron-hole rich species active in the electrocatalytic water oxidation. J. Am. Chem. Soc. **143**(32), 12524–12534 (2021). https://doi.org/10.1021/jacs.1c01655
61. A.S. Aricò, A.K. Shukla, H. Kim, S. Park, M. Min et al., An XPS study on oxidation states of Pt and its alloys with Co and Cr and its relevance to electroreduction of oxygen. Appl. Surf. Sci. **172**(1–2), 33–40 (2001). https://doi.org/10.1016/S0169-4332(00)00831-X
62. L. Zhang, H. Jang, H. Liu, M.G. Kim, D. Yang et al., Sodium-decorated amorphous/crystalline RuO_2 with rich oxygen vacancies: a robust pH-universal oxygen evolution electrocatalyst. Angew. Chem. Int. Ed. **60**(34), 18821–18829 (2021). https://doi.org/10.1002/anie.202106631
63. I. Ardelean, M. Peteanu, R. Ciceo-Lucacel et al., Structural investigation of CuO containing strontium-borate glasses by means of EPR and IR spectrometry. J. Mater. Sci. Mater. Electron. **11**, 11–16 (2000). https://doi.org/10.1023/A:1008943901463
64. A. Martınez-Arias, M. Fernández-Garcıa, O. Gálvez, J.M. Coronado, J.A. Anderson et al., Comparative study on redox properties and catalytic behavior for CO oxidation of CuO/CeO_2 and CuO/$ZrCeO_4$ catalysts. J. Catal. **195**(1), 207–216 (2000). https://doi.org/10.1006/jcat.2000.2981
65. Y. Wang, T. Zhou, K. Jiang, P. Da, Z. Peng et al., Reduced mesoporous Co_3O_4 nanowires as efficient water oxidation electrocatalysts and supercapacitor electrodes. Adv. Energy Mater. **4**(16), 1400696 (2014). https://doi.org/10.1002/aenm.201400696
66. M.C. Biesinger, B.P. Payne, A.P. Grosvenor, L.W.M. Lau, A.R. Gerson et al., Resolving surface chemical states in XPS analysis of first row transition metals, oxides and hydroxides: Cr, Mn, Fe, Co and Ni. Appl. Surf. Sci. **257**(7), 2717–2730 (2011). https://doi.org/10.1016/j.apsusc.2010.10.051

67. W. Moschkowitsch, O. Lori, L. Elbaz, Recent progress and viability of PGM-free catalysts for hydrogen evolution reaction and hydrogen oxidation reaction. ACS Catal. **12**(2), 1082–1089 (2022). https://doi.org/10.1021/acscatal.1c04948
68. Y. Wang, H. Yan, H. Fu, Recent advances and modulation tactics in Ru- and Ir-based electrocatalysts for PEMWE anodes at large current densities. eScience **5**(3), 100323 (2025). https://doi.org/10.1016/j.esci.2024.100323
69. H.N. Nong, T. Reier, H.-S. Oh, M. Gliech, P. Paciok et al., A unique oxygen ligand environment facilitates water oxidation in hole-doped IrNiOx core–shell electrocatalysts. Nat. Catal. **1**(11), 841–851 (2018). https://doi.org/10.1038/s41929-018-0153-y
70. S. Geiger, O. Kasian, B.R. Shrestha, A.M. Mingers, K.J.J. Mayrhofer et al., Activity and stability of electrochemically and thermally treated iridium for the oxygen evolution reaction. J. Electrochem. Soc. **163**(11), F3132–F3138 (2016). https://doi.org/10.1149/2.0181611jes
71. A. Gorczyca, V. Moizan, C. Chizallet, O. Proux, W. Del Net et al., Monitoring morphology and hydrogen coverage of nanometric Pt/γ-Al_2O_3 particles by In Situ HERFD–XANES and quantum simulations. Angew. Chem. Int. Ed. **53**(46), 12426–12429 (2014). https://doi.org/10.1002/anie.201403585
72. F.-Y. Yu, Z.-L. Lang, L.-Y. Yin, K. Feng, Y.-J. Xia et al., Pt-O bond as an active site superior to Pt^0 in hydrogen evolution reaction. Nat. Commun. **11**(1), 490 (2020). https://doi.org/10.1038/s41467-019-14274-z
73. A. Grimaud, O. Diaz-Morales, B. Han, W.T. Hong, Y.-L. Lee et al., Activating lattice oxygen redox reactions in metal oxides to catalyse oxygen evolution. Nat. Chem. **9**(5), 457–465 (2017). https://doi.org/10.1038/nchem.2695
74. T. Kim, S.B. Roy, S. Moon, S. Yoo, H. Choi et al., Highly dispersed Pt clusters on F-doped tin(IV) oxide aerogel matrix: an ultra-robust hybrid catalyst for enhanced hydrogen evolution. ACS Nano **16**(1), 1625–1638 (2022). https://doi.org/10.1021/acsnano.1c10504
75. J. Greeley, T.F. Jaramillo, J. Bonde, I.B. Chorkendorff, J.K. Nørskov, Computational high-throughput screening of electrocatalytic materials for hydrogen evolution. Nat. Mater. **5**(11), 909–913 (2006). https://doi.org/10.1038/nmat1752

 https://doi.org/10.1007/s40820-025-01845-7